Research Square

Preprints are preliminary reports that have not undergone peer review.
They should not be considered conclusive, used to inform clinical practice,
or referenced by the media as validated information.

Crustal heat supply beneath Zibo constrained by borehole observations and alternative thermal property models

Yuzhong Liao
Chinese Academy of Geological Sciences
Wei Zhang
Chinese Academy of Geological Sciences
Long Li
lilong123iheg@126.com

Chinese Academy of Geological Sciences
Tonglin Li
Sichuan Earthquake Administration
Zhidong Jiang
Geological Environment Monitoring Institute of Jiangxi Geological Survey and Exploration Institute

Research Article

Keywords: Zibo, terrestrial heat flow, crustal thermal structure, thermal conductivity, radiogenic heat production

Posted Date: November 10th, 2026

DOI: https://doi.org/10.21203/rs.3.rs-11416997/v1

License: This work is licensed under a Creative Commons Attribution 4.0 International License.
Read Full License

Additional Declarations: No competing interests reported.

Crustal heat supply beneath Zibo constrained by borehole observations and alternative thermal property models

Yuzhong Liao[1,2], Wei Zhang[1,2], Long Li[1,2*], Tonglin Li[3], Zhidong Jiang[4,5]

[1] *Institute of Hydrogeology and Environmental Geology, Chinese Academy of Geological Sciences, Shijiazhuang 050061, China*

[2] *Technology Innovation Center for Geothermal & Hot Dry Rock Exploration and Development, Ministry of Natural Resources, Shijiazhuang 050061, China*

[3] *Sichuan Earthquake Administration, Chengdu 610000, China*

[4] *Geological Environment Monitoring Institute of Jiangxi Geological Survey and Exploration Institute, Jiangxi, China*

[5] *Jiangxi Provincial Coalfield Geological Exploration and Research Institute, Jiangxi, China*

Corresponding author: Long Li (lilong123iheg@126.com).

Abstract

The partitioning of crustal radiogenic heating and basal heat input beneath Zibo remains uncertain. We assess how crustal structure and thermal properties affect deep temperatures and heat partitioning, using the published Linyi model as a regional reference. Temperature profiles from borehole ZB-ZK1, thermal-property data for 92 regional rock samples and a geoscience transect were combined in two one-dimensional conductive models based on P-wave velocity and lithological analogues. The models share upper boundary conditions, including the adopted terrestrial heat flow of 64.6 mW m^{-2}, and incorporate temperature-dependent conductivity. Effective upper-crustal conductivity was calibrated by assigning 585°C to the published magnetic-source bottom at 24.74 km. The 100–200 m borehole interval yields a geothermal gradient of 17.03°C km^{-1}. V and L1 yield Moho temperatures of 693.7 and 678.3°C at 31.06 km, crustal radiogenic contributions of 21.26 and 28.65 mW m^{-2} and residual Moho heat flows of 43.34 and 35.95 mW m^{-2}, respectively. These Moho heat flows bracket the published Linyi value of 38.88 mW m^{-2}, reversing the inferred Zibo–Linyi ranking between scenarios. Matching the common deep temperature therefore constrains geotherms without uniquely determining the crustal and basal heat contributions, which depend on prescribed layering and radiogenic heat production. These results provide a conductive baseline for geothermal assessment at Zibo and identify formation-specific thermal properties and deep equilibrium temperatures as priorities for regional heat-supply comparisons.

Keywords: Zibo; terrestrial heat flow; crustal thermal structure; thermal conductivity; radiogenic heat production

1 Introduction

Geothermal resources supply heat for buildings, agriculture and industry at temperatures below those required for conventional geothermal power generation. Global surveys document widespread direct use, including space and district heating (Lund and Toth 2021). Resource suitability depends on temperature, sustainable discharge and fluid chemistry (Lund et al. 2022). Geological classifications distinguish conduction-dominated sedimentary and crystalline settings from convection-dominated systems and relate exploration strategies to heat sources, migration pathways and reservoir properties (Moeck 2014). Assessing a geothermal resource therefore requires both the regional thermal regime and the processes that concentrate and transport heat.

Low- to medium-temperature geothermal resources are widespread in Chinese sedimentary basins and mountain fault zones and support extensive direct use (Zhu et al. 2015; Wang et al. 2017). Eastern China contains porous sandstone, karst carbonate and fractured crystalline reservoirs controlled by regional structure and local reservoir–caprock relationships (He et al. 2023). Estimates of deeper resources depend on the temperature–depth relation and on the technical and economic conditions governing heat recovery (Ma 2023). Conductive models constrain the thermal background, while hydraulic characterization is needed to assess well productivity and recoverable heat.

Zibo and Linyi provide contrasting structural settings for evaluating regional thermal models. Zibo lies at the northern basin–uplift transition of western Shandong, adjacent to the Jiyang Depression; the Linyi geothermal field follows branches of the Yishu segment of the Tan-Lu fault system (Li et al. 2013; Liao et al. 2023). The regional framework records basin subsidence and uplift, stratigraphic and crustal detachments, and superimposed extensional and strike-slip deformation (Li et al. 2009; Qi and Yang 2010). Cretaceous changes in deformation along the middle Tan-Lu system (Zhang et al. 2003) and Meso-Cenozoic cooling and exhumation (Yang et al. 2020) provide further context for local

thermal assessment. The comparison addresses structural and reservoir differences within this regional framework.

Terrestrial heat-flow observations provide the regional context. Chinese compilations show marked spatial variability and uneven geographical coverage and data quality (Jiang et al. 2019; Wang et al. 2024). Deep crystalline boreholes in the southeastern North China Craton show the effects of groundwater circulation, shallow thermal perturbations and conductivity selection on heat-flow estimates (Jiang et al. 2016). Measurements along the southern Tan-Lu sector indicate a broadly normal thermal background with local variation (Wang et al. 2019), demonstrating that fault proximity alone does not establish a regional heat-flow anomaly. These observations provide regional context for Zibo and Linyi.

Reservoir studies document how local geothermal conditions develop within the regional thermal regime. Northwestern Shandong contains sandstone reservoirs and mudstone aquitards with structurally variable burial depths (Liu et al. 2023). Karst hydrothermal enrichment in the Bohai Bay Basin depends on heat supply, reservoir properties and hydraulic connectivity, with different controls at basin margins and buried hills (Li et al. 2024). Studies in Jiaodong identify intersecting faults and local heat redistribution (Shi et al. 2022), while hydrochemical and isotopic evidence from northern Jinan indicates meteoric recharge, deep circulation and mixing (Wang et al. 2015; Gao et al. 2023). These processes guide interpretation of the Zibo reservoir system.

Previous Zibo studies constrain reservoir geometry and groundwater circulation. Southern Zhangdian investigations identified meteoric recharge, fault-controlled circulation and locally convective temperature profiles (Yang et al. 2005). The wider geothermal field contains an Ordovician carbonate reservoir that deepens northward beneath sedimentary cover (Xiang et al. 2009). Electrical investigations resolved buried reservoir geometry and faults in the Zibo synclinal basin (Yang 2020). These findings explain local heat storage and redistribution. The present analysis examines the

conductive background and its partition between crustal radiogenic heat production and basal heat input.

The Linyi thermal study combined borehole temperatures, rock thermal properties and a geoscience transect to estimate crustal heat production, basal heat flow and Moho temperature (Liao et al. 2023). Its representative column used 64.9 mW m^{-2}, close to the 64.6 mW m^{-2} adopted for Zibo, despite a higher geothermal gradient and lower shallow conductivity. The two values describe different borehole intervals and are not field-wide averages. The interpretation of a high thermal background at Linyi also incorporated other wells, regional observations and crustal–mantle structure. Together with layered thermal modelling in Jinggangshan (Liao et al. 2022), this work provides a basis for examining the Zibo thermal regime under alternative deep-property assignments.

Alternative crustal parameterizations can produce different heat budgets under similar upper thermal boundary conditions (Lachenbruch 1970). A prescribed deep temperature narrows the range of geotherms while leaving the crustal and basal contributions dependent on the heat-production profile. We quantify this dependence at Zibo before comparing its basal heat supply with Linyi. The comparison also requires an assessment of the adopted rock analogues: age, lithology and sampling region covary, and thermal resistance and radiogenic heat production affect different components of the conductive model (Jaupart et al. 2016).

We combine temperature observations from the 200 m ZB-ZK1 borehole, regional rock measurements and the Xiangshui–Mandula geoscience transect (Ma et al. 1991a) in two one-dimensional crustal models. The velocity-based model (V) derives deep heat production from P-wave velocity; the lithological analogue model (L1) uses regional rock properties and an alternative crustal subdivision. Both models retain the same upper boundary conditions. A magnetic-source bottom depth from the Global Curie Depth Model defines the depth assigned to 585°C (Li et al. 2017), and calibration adjusts only the effective upper-crustal reference conductivity. The published Linyi column (Liao et al. 2023) is retained as the regional comparison.

The analysis evaluates how crustal geometry and thermal-property assignments affect calibrated conductivity, temperature profiles and crustal–basal heat partitioning beneath Zibo. Comparison with the published Linyi column tests the stability of the regional basal heat-flow ranking. We examine the upper boundary conditions, regional rock analogues and magnetic-temperature assignment separately to identify the observations that can distinguish the alternative models.

2 Geological and geothermal setting

Zibo is located in central Shandong Province, within the eastern North China Craton (Fig. 1). At the regional scale, the Qihe–Guangrao fault separates the West Shandong Rise from the Jiyang Depression. The former is part of the elevated periphery of the Bohai Bay Basin, whereas the latter belongs to the basin system. Archean–Paleoproterozoic crystalline basement is overlain by younger sedimentary and locally volcanic successions (Li et al. 2013).

The regional map identifies the North China depression, Luxi terrane, Jiaobei terrane and Jiaonan-Weihai orogenic belt using the tectonic labels of the Linyi map, modified after Fang's dissertation (Liao et al. 2023; Fang 2006) (Fig. 1). ZB-ZK1 lies near the northern margin of the Luxi domain. The published LHT-ZK1 location is also on the Luxi side of the main eastern division. These positions define the regional setting of the borehole comparison; the Yishu fault is shown as a multibranch fault system.

The regional transects and boreholes have different spatial support. In the retained map geometry, ZB-ZK1 lies approximately 6.7 km from the Zibo transect and the nominal LHT-ZK1 location approximately 10.3 km from the Linyi transect. These are approximate map distances, conditional on the available datum registration. The Zibo transect crosses the northern basin–uplift division, whereas the Linyi transect extends across the main eastern division towards the Jiaonan-Weihai side. Neither crossing assigns the associated borehole to the unit on the opposite side. Transferring these regional sections to the well-centred thermal columns is therefore an explicit assumption. Tectonic divisions do

not by themselves identify active or hydraulically transmissive faults; Linyi's relation to the Yishu branches follows its published geological interpretation (Liao et al. 2023).

The Zhangdian sector of Zibo occupies the northern margin of the central Shandong uplift, where low hills grade into the piedmont plain. In southern Zhangdian, Ordovician carbonates and Carboniferous, Permian and Triassic–Jurassic strata are largely concealed beneath Quaternary deposits, with local bedrock exposures (Yang et al. 2005). The folded and faulted succession contains an Ordovician reservoir that deepens northward beneath younger cover (Xiang et al. 2009). The conceptual reservoir model (Xu and Ren 2016) illustrates Quaternary deposits, Jurassic, Triassic and Carboniferous sandstones, and Ordovician limestone (Fig. 2b). Meteoric recharge from the southeastern hills and groundwater circulation near the Wangmushan and Nanding faults redistribute the upward terrestrial heat flow. We use this conceptual geometry to describe reservoir and circulation relationships; the formation contacts at ZB-ZK1 are assessed separately.

The Zhangdian study distinguished Quaternary pore water, fracture water in the Permian–Jurassic sandstone succession, and karst water in Ordovician carbonates (Yang et al. 2005). The regionally extensive Ordovician aquifer receives recharge from carbonate outcrops in the southern hills, with groundwater moving towards the covered piedmont. The younger sedimentary succession provides cover over the carbonate reservoir while also containing sandstone-hosted fracture-water units. Xiang and co-authors reported Ordovician reservoir-top depths of approximately 300–1600 m across their geothermal field, generally increasing northward (Xiang et al. 2009). Electrical interpretations elsewhere in the Zibo synclinal basin likewise indicate buried carbonate interfaces and fault-related changes in reservoir depth, although cultural interference limits some shallow-interface interpretations (Yang 2020). These reservoir depths and the shallow Quaternary-cover thickness at ZB-ZK1 describe different geological interfaces.

Faults influence groundwater flow in different ways. In southern Zhangdian, the central Nanding fault zone was described as hydraulically connected, whereas its end segments and parts of the

Mansihe fault were weakly transmissive. The Wangmushan fault separates contrasting groundwater heads, while fractured sectors near Tangjiashan were interpreted as enhanced-flow pathways (Yang et al. 2005). Temperature profiles in that study included conductive upper intervals and deeper intervals affected by circulation. Together with the hydrochemical evidence, these observations support meteoric recharge and structurally influenced water movement, while indicating that hydraulic connectivity varies among faults and along individual fault segments.

The authors' project compilation records five geothermal manifestations with water temperatures of 32–54°C (Fig. 2a): HR-1 at Huangjin International (54°C), the Tangjiazhuang spring ZBWQ-A001 (41.5°C), the Nanding Fourth Grinding Wheel Factory water-supply well ZBDR-B001 (34°C), the Xiaotun well XTDR-1 (38°C), and HR-2 northwest of Shuangyang (32°C). The HR-2 and XTDR-1 assignments were checked against the locations and well records in the original Zhangdian study (Xiang et al. 2009). These sites establish the regional hydrothermal context. ZB-ZK1 supplies a separate shallow temperature record; its information sheet identifies Quaternary clay and sandstone and Ordovician dolomitic limestone without recording their contact depth. The deeper regional interpretation is drawn from the geoscience transect (Ma et al. 1991a); its use for thermal-property analogues is described in Section 3.

Fig. 3 shows the Ningjin–Jiyang–Zibo part of the Xiangshui–Mandula geoscience transect. The broader northwest–southeast segment from Zibo towards Yingxian crosses the Jiyang Depression, Cangxian Uplift and Jizhong Depression. Its explanatory notes describe Paleogene Kongdian, Shahejie and Dongying deposits, followed by the Guantao and Minghuazhen formations and Quaternary sediments. Faulted depressions and intervening uplifts produce lateral changes in sediment thickness, and listric normal faults were interpreted to flatten towards intracrustal detachments (Ma et al. 1991a). This inherited structural framework guides the column geometry and analogue selection; the present study calculates its conditional thermal consequences.

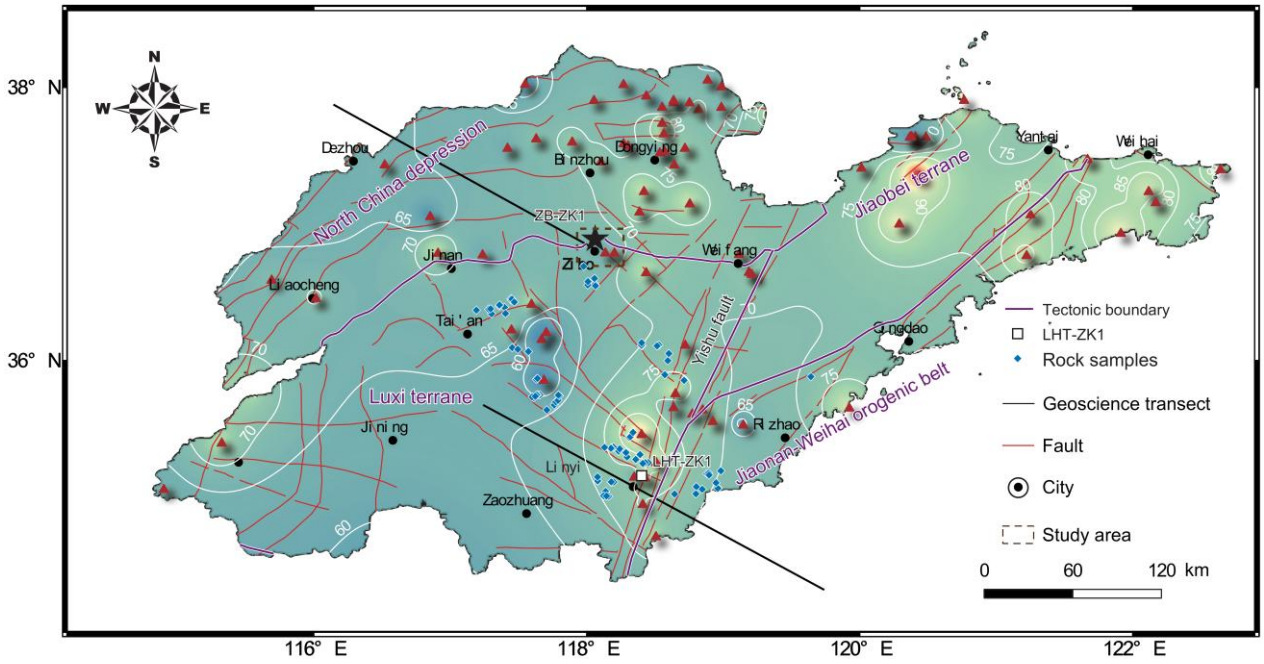


Fig. **1.** Regional geological setting and terrestrial heat-flow distribution in Shandong. Star, ZB-ZK1; square, LHT-ZK1; blue diamonds, adopted rock samples; red triangles, heat-flow stations; white contours, terrestrial heat flow (mW m^{-2}); purple lines, tectonic boundaries; red lines, faults; black profiles, geoscience transects. Regional base modified after (Liao et al. 2023; Fang 2006).

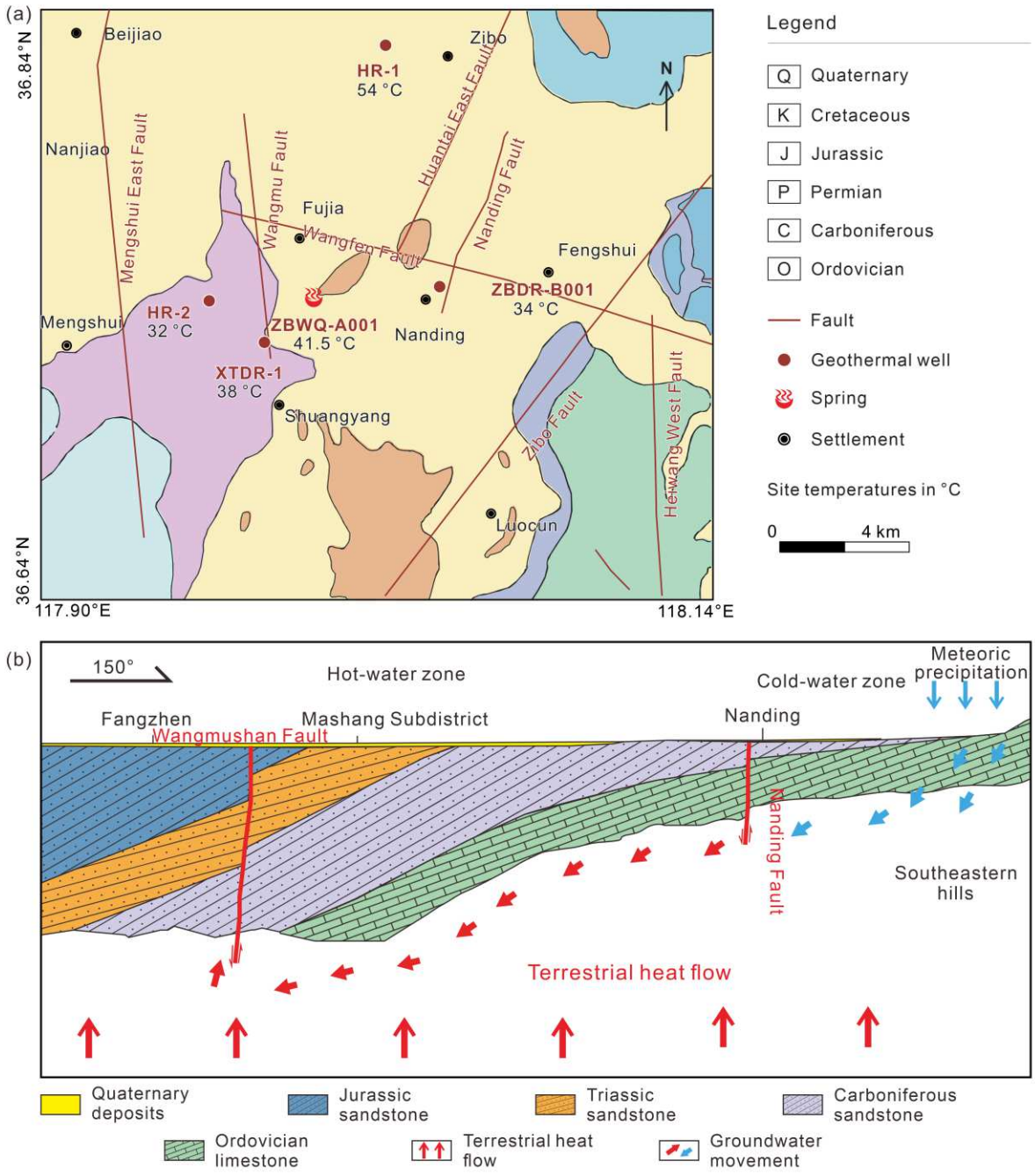


Fig. **2.** Geological setting and hydrogeological model of the Zhangdian geothermal field (modified after (Zuo et al. 2018)); site correspondence after (Xiang et al. 2009). b Conceptual reservoir and groundwater-circulation model, modified after (Xu and Ren 2016).

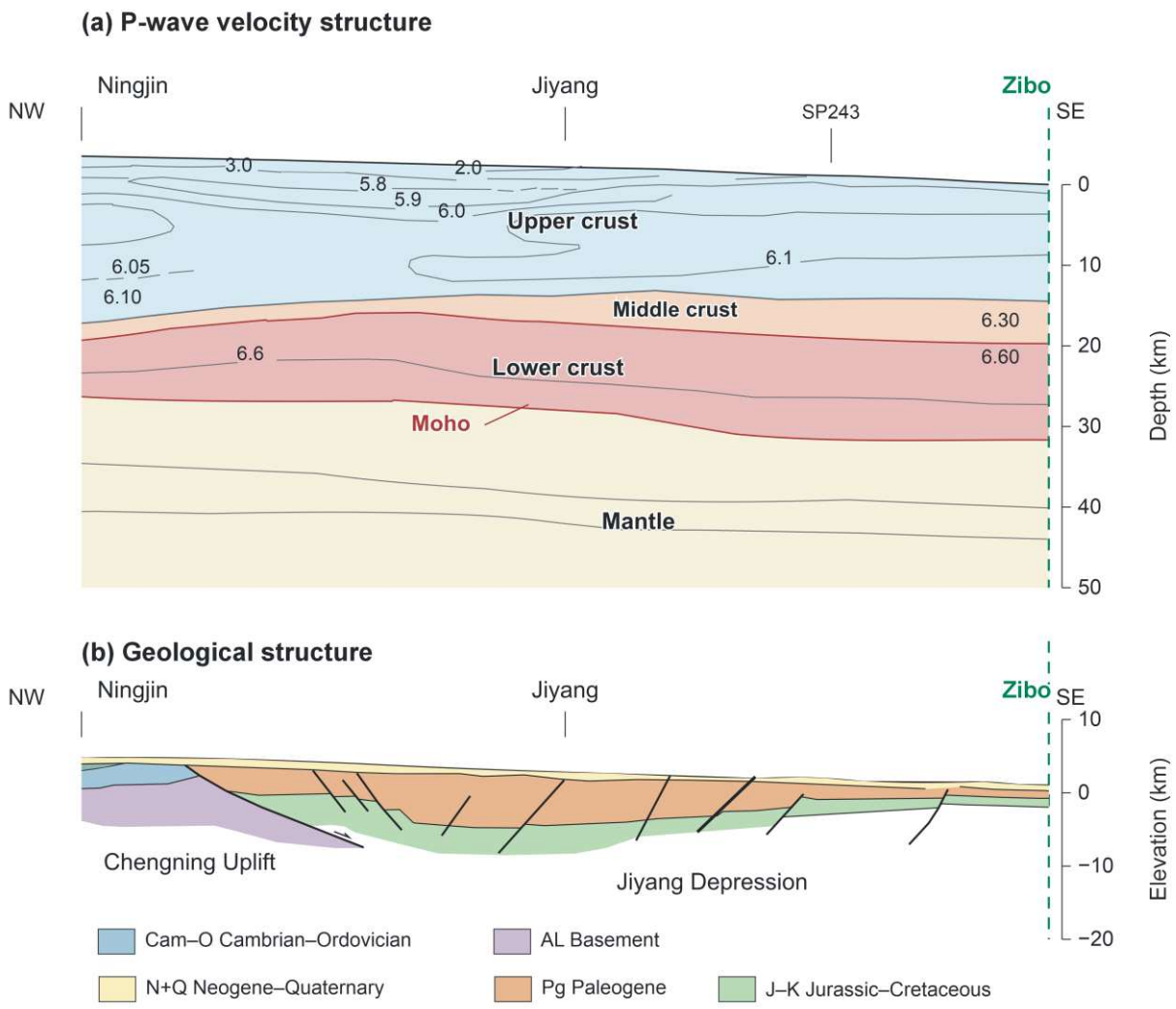


Fig. **3.** Seismic and geological structure along the Ningjin–Zibo transect, modified after (Ma et al. 1991b). a P-wave velocity structure. b Geological section. Green dashed lines mark Zibo. V_p, P-wave velocity (km s^{-1}).

3 Data and methods

3.1 Shallow borehole temperature monitoring

Temperature records for ZB-ZK1 at the Zibo pharmaceutical plant were extracted from the Origin workbook and checked against the source spreadsheets. The borehole defines the upper thermal boundary conditions of the Zibo models. Fig. 4 combines the interpreted lithology, temperature observations and geothermal gradient.

The well inventory places ZB-ZK1 at 118°04′E, 36°53′N and records a monitoring depth of 200 m. Repeated temperature profiles were used to evaluate short-term thermal stability at the borehole.

198 Borehole temperatures were measured using the sensor-cable method described in the Jinggangshan
199 study (Liao et al. 2022). The system comprised WD-016A embedded temperature sensors connected to
200 a TD-016C data-acquisition unit. The published configuration used 11-mm-diameter sensors
201 embedded in a 12-mm-diameter polyvinyl chloride (PVC) cable, with a stated accuracy of 0.1°C over
202 0–80°C. For ZB-ZK1, the archived profiles contain 26 depth labels at 5 m intervals from 0 to 50 m and
203 10 m intervals from 50 to 200 m, consistent with the published cable configuration. Nine profiles were
204 recorded between 17:12:07 on 14 May and 17:39:44 on 15 May 2022. The field inventory records that
205 the well had remained undisturbed for more than one year before these measurements. The repeated
206 profiles were used to assess short-term variability; the geothermal gradient was evaluated over 100–
207 200 m using the 11 available depth levels in that interval.

208 **3.2 Conductive interval and adopted thermal properties**

209 Ordinary least-squares (OLS) regression of mean temperature against depth was applied to the 100–
210 200 m interval. Geothermal gradient (G) is expressed in °C km^{-1}, thermal conductivity (k) in W m^{-1}
211 K^{-1} and terrestrial heat flow (q) in mW m^{-2}, with $q = kG$. The inventory values $G = 17$ and $k = 3.8$ give
212 $q = 64.6$, which is retained as the prescribed upper boundary. The independently fitted gradient
213 provides a check on the archived temperature calculation.

214 The assigned conductivity of 3.8 W m^{-1} K^{-1} is a limestone analogue from the source compilation.
215 The ZB-1 field sheet records Quaternary clay and sandstone above Ordovician dolomitic limestone at
216 the monitoring-well location. The 2022 working sheet interprets the thermal-analysis interval as
217 Ordovician limestone. Limestone, dolomitic limestone and dolostone were distinguished when
218 selecting the measured rock analogues.

219 The shallow stratigraphic column in Fig. 4 uses the Quaternary thickness range of 1.24–25.6 m
220 reported for southern Zhangdian by (Yang et al. 2005) (p. 59). The contact range provides regional
221 stratigraphic context for the schematic column. The 100–200 m temperature-fitting interval and 100 m

thermal anchor are retained. This shallow contact assignment does not change the kilometre-scale sedimentary package or the subsequent heat-budget calculation.

All ZB-ZK1 temperature measurements were retained. The local-gradient profile uses centred differences of interval mean temperature at internal nodes and one-sided differences at the endpoints (Fig. 4), without smoothing. The regression standard error measures the precision of the fitted slope for these observations; conductivity selection, groundwater circulation and spatial representativeness are assessed separately.

The adopted conductivity was audited against the 2022 Shandong sample database using its 183 unique sample identifiers. Sample identifiers, source-assigned lithology and age, measured properties and quality flags were retained (Table 1). The publication tables omit sample coordinates; a complete coordinate-bearing version is preserved by the authors. The 25-point Zibo collection register was linked to the laboratory database by sample identifier to avoid duplicate counting. Three samples explicitly located in Zibo and classified as limestone have conductivities of 2.6620, 2.8713 and 3.9957 W m^{-1} K^{-1}. Their arithmetic mean is 3.1763; restricting the group to the two Ordovician samples gives 3.4335. The four Ordovician limestone samples across the Shandong database average 3.6850. The model retains the inventory conductivity of 3.8 W m^{-1} K^{-1}; the sample means provide lithological comparisons. The local Ordovician mean provides a stratigraphically relevant comparison but is based on two surface samples, not this borehole. The archive includes conductivity observations and radioelement data previously reported in the Linyi studies (Liao et al. 2023; Liao et al. 2025); sample references are listed in the sample register (Additional file 1).

Table 1. Regional carbonate samples used for the conductivity comparison

Sample ID	Lithology	k (W m⁻¹ K⁻¹)	A (μW m⁻³)	Source row
ZBDZ-B001	Ordovician limestone	3.9957	—	182
ZBDZ-B002	Cambrian limestone	2.6620	—	33
ZBDZ-B003	Ordovician limestone	2.8713	—	181
ZBDZ-A003	Dolostone	—	0.5705	30
ZBDZ-A004	Dolostone	3.0333	0.8189	31

Note: k, thermal conductivity; A, volumetric radiogenic heat production; —, property not adopted. Source: 2022 Shandong rock archive.

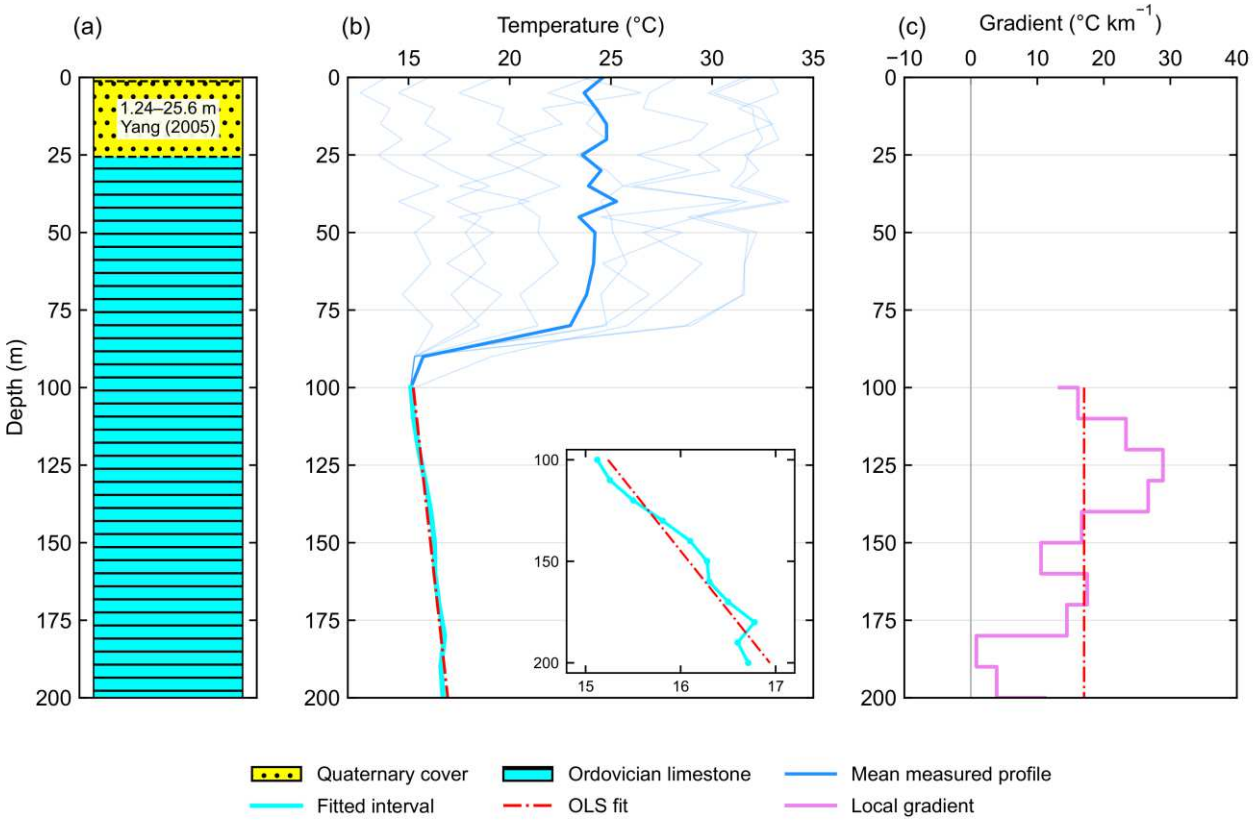


Fig. **4.** Shallow stratigraphy, temperature and geothermal gradient at ZB-ZK1. a Schematic stratigraphy showing the southern Zhangdian Quaternary thickness range of 1.24–25.6 m (Yang et al. 2005). b Repeated temperature profiles (n = 9), mean profile and OLS fit over 100–200 m (inset). c Local geothermal gradient. OLS, ordinary least squares. The panels share a depth scale.

3.3 Seismic and geological constraints

The Zibo profile spreadsheet supplies ten depth–P-wave velocity nodes spanning approximately 0.31–43.79 km. The original negative depths were converted to positive downward depths; kilometres

and kilometres per second were inferred from the companion geoscience transect. These regional nodes provide the one-dimensional velocity input transferred to the ZB-ZK1 thermal column.

The seismic and geological panels in Fig. 3 were adapted from the journal transect (Ma et al. 1991b); the map and explanatory notes (Ma et al. 1991a) provide the regional geological and crustal-layering context. The panels were aligned at Ningjin, Jiyang and Zibo over their common interval, retaining the original curves, velocity annotations and depth or elevation references. The velocity horizons and Moho define the seismic color domains, while the geological section retains the source stratigraphic interpretation. This regional registration provides the structural framework for the thermal models.

Model V assigns the sedimentary-package base to 6 km, with 5 and 7 km alternatives; this kilometre-scale package is distinct from the shallow Quaternary cover. Its upper-crustal base is the 14.596 km velocity node, consistent with the explanatory notes' regional upper-crustal thickness of 12–15 km. The middle/lower-crust boundary is assigned to 19.565 km, near the 6.3–6.6 km s^{-1} increase. This yields a middle crust approximately 4.97 km thick, outside the notes' regional 7–10 km range, which is examined through separate 7 and 10 km thickness scenarios. The 31.056 km node at 8.0 km s^{-1} is the reference Moho candidate. The 27.019 km node at 7.2 km s^{-1} is tested as a transition-top alternative, rather than assumed to be the same interface. These assignments are thermal-model scenarios; neither the regional thickness ranges nor individual velocity nodes uniquely determine local petrological boundaries. The two deeper mantle nodes are retained in the archive without assigning a lithosphere–asthenosphere boundary.

3.4 Heat production and temperature-dependent conductivity

We model one-dimensional steady-state conduction from the 0.1 km temperature anchor to the adopted Moho, neglecting fluid advection, lateral heat transport and transient effects. The upper boundary is the nine-profile mean temperature of 15.1222°C and the prescribed heat flow of 64.6 mW m^{-2}. The heat budget covers the interval below 100 m, with no radiogenic correction assigned above

the anchor. Let z denote downward depth, q upward conductive heat flow and A volumetric radiogenic heat production. Conservation of energy and Fourier's law give

$$dq/dz = -A;\ dT/dz = q/k. \quad (1)$$

For a layer of thickness D and constant volumetric radiogenic heat production (A), heat conservation gives

$$q_1 = q_0 - AD. \quad (2)$$

In model V, P-wave velocity (V_p) determines crystalline-crust heat production through the empirical relation used in the Linyi study (Liao et al. 2023), following (Čermák et al. 1990):

$$A = 1.35\, exp[1.5(6 - V_p)]. \quad (3)$$

Here V_p is the mean of the original seismic-interval boundary velocities in km s^{-1} and A is in μW m^{-3}. Splitting a seismic interval at a thermal-property boundary does not change its original heat-production assignment. Regional surface-rock U–Th–K records are available, but they do not establish representative heat production for the target borehole interval or deep crust. The only Zibo limestone with a listed heat-production result, ZBDZ-B003, has A = 21.5004 μW m^{-3} and is explicitly flagged as anomalous in the source database. Its unflagged conductivity was retained in the conductivity comparison, while its flagged A was not assigned to the entire sedimentary package. Unflagged Zibo dolostones yield 0.5705 and 0.8189 μW m^{-3}, but represent a different lithology. Sedimentary A is therefore retained as a limestone-analogue scenario of 0.7 μW m^{-3}, with 0.3–1.4 μW m^{-3} alternatives tested below; it is not represented as a measurement from ZB-ZK1. The inventory identifies the 0.7 μW m^{-3} sedimentary assignment as the Linyi limestone analogue (Liao et al. 2023); its use beneath Zibo remains conditional.

Thermal conductivity k(T,z) is expressed in terms of reference conductivity (k_0), a temperature coefficient (b) and a depth coefficient (c):

$$k(T,z) = k_0(1 + cz)/(1 + bT). \quad (4)$$

For model V, the initial upper-, middle- and lower-crustal k_0 values are 3.0, 2.8 and 2.6 W m^{-1} K^{-1}, respectively. The primary calibration adjusts only the upper-crustal value, giving 2.2177 W m^{-1} K^{-1} at the magnetic-depth target (Li et al. 2017). The temperature coefficients b are 0.0015, 0.0001 and 0.0001°C^{-1} for the upper, middle and lower crust, and the depth coefficient c is 0.0015 km^{-1}, following the crystalline-crust conductivity correction used in the Linyi study (Liao et al. 2023). Equation (4) uses z in kilometres and T in degrees Celsius. The crystalline-crust reference conductivities are analogue assignments; their temperature dependence is lithology dependent (Vosteen and Schellschmidt 2003). The sedimentary package retains a constant conductivity of 3.8 W m^{-1} K^{-1}, with cover-property alternatives evaluated separately.

3.5 Numerical solution and sensitivity analysis

For a constant representative conductivity within each layer, the reference recurrence is

$$T_1 = T_0 + (q_0 D - AD^2/2)/k. \quad (5)$$

The primary V and L1 solutions integrate continuous k(T,z). Equation (5) is retained to compare this solution with the inherited layer-bottom-temperature rule and a layer-mean-temperature alternative. Its units are numerically consistent for D in km, q in mW m^{-2}, A in μW m^{-3} and k in W m^{-1} K^{-1}. The reference article's mean-temperature description and the inherited layer-bottom implementation are evaluated separately rather than treated as equivalent numerical procedures.

Defining $S = (q_0 D - AD^2/2)/[k_0(1 + cz_1)]$, the layer-bottom rule has the explicit solution $T_1 = (T_0 + S)/(1 - bS)$, subject to a positive denominator. For the continuous model, integrating q/k with the same layer heat production gives an independent analytic solution. Constant-property analytic benchmarks, direct quadrature checks, conservation of the heat budget and convergence under layer subdivision were used to verify the implementation. Values outside a scenario's model depth were left undefined rather than extrapolated.

Sensitivity tests vary the upper-boundary heat flow, upper-crustal k_0 and all-layer A separately by ±10% around the calibrated V model. Conductivity is held at its calibrated value after each perturbation, allowing the thermal response to be evaluated without refitting the deep-temperature target. These are deterministic sensitivity ranges. Magnetic-grid sampling and the assigned magnetic-source temperature are tested separately, with the measured sample values unchanged.

3.6 Regional rock analogues and alternative crustal layering

We constructed a second thermal model using regional rock measurements with the same ZB-ZK1 boundary temperature and heat flow as the velocity-based model. The All worksheet of the Shandong sample database contains 183 unique sample identifiers. After excluding each property's original anomalous flags, 153 conductivity values and 74 heat-production values remain. Conductivity and heat production were screened separately; missing values were not replaced by zero, and a conductivity flag did not automatically exclude a valid heat-production result. The 25-sample Zibo register is a subset of the same collection. Original classifications, flags and source rows remain in the source archive; the accompanying sample table displays only properties used by the reference models and predefined rock-analogue comparisons. Fourteen adopted conductivity observations were individually published in Table 2 of (Liao et al. 2023). Four adopted heat-production values use the sample-level radioelement and density data in its Table 7; individual calculations are kept distinct from published lithology-group means.

Table 2 and Fig. 5 summarize the measured rock analogues by lithological group. For each property, we calculated the number of adopted measurements, arithmetic mean, sample standard deviation (SD) and observed range. Conductivity and heat production have separate counts because their sample subsets differ. SD describes sample dispersion within the sampled groups. We checked the source heat-production values using $A = \rho(0.0952U + 0.0256Th + 0.0348K)$, where ρ is density in g cm^{-3}, U and Th are uranium and thorium concentrations in ppm, and K is potassium concentration in

weight percent. The calculation reproduces all 75 numerical entries to rounding precision; the original exclusion flags were retained.

The transect describes ancient metamorphic rocks and intrusions in the upper crust, heterogeneous migmatitic and amphibolite-facies rocks in the middle crust, and granulite-facies rocks in the lower crust (Ma et al. 1991a) (pp. 31 and 56). These regional descriptions guide the lithological analogues. Gneiss represents the upper crust. The middle crust contains equal assumed volume fractions of leptynite and meta-amphibolite, with A mixed arithmetically and k harmonically for a series arrangement. The prescribed fractions are independent of sample counts. Leptynite and granulite retain their separate source classifications.

The lower-crustal analogue is TAN-9, the only explicitly classified granulite sample, with $k = 2.6313$ W m^{-1} K^{-1} and $A = 0.6831$ μW m^{-3}. It is a near-surface sample from Tai'an, approximately 103 km from ZB-ZK1. Its use as a lower-crustal analogue is therefore an extrapolation. Evidence for a generally more mafic lower crust provides broad compositional context but does not determine the composition beneath Zibo (Christensen and Mooney 1995). Laboratory conductivity defines k_0 for the lithological analogues, with temperature and depth corrections applied through Eq. (4).

Model V uses the velocity-based property assignment and reference thermal boundaries. Model L1 combines the regional rock analogues with upper- and middle-crustal bases at 14 and 22 km and the common Moho at 31.056 km. Its total upper-, middle- and lower-crustal thicknesses are 14, 8 and 9.056 km, within the transect's regional ranges of 12–15, 7–10 and 8–11 km. The upper-crustal thickness includes the 0–6 km cover, although computation begins at 0.1 km. Both models use continuous k(T,z) integration and the prescribed upper-boundary heat flow of 64.6 mW m^{-2}. Table 3 summarizes the calibrated L1 assignments. Because V and L1 change both layer geometry and property assignments, their comparison tests alternative crustal scenarios rather than isolating one parameter's effect.

The adopted dataset contains 92 samples: 87 conductivity values, 43 heat-production values and 38 paired records. Only properties used in the reference models or predefined analogue comparisons are included. Collection records identify 51 surface samples and leave the collection mode unspecified for 41 samples. The sample register lists identifiers, lithology, age, adopted thermal properties and references (Additional file 1). Sample coordinates are omitted from the publication tables and retained in the author archive. The map uses the nominal World Geodetic System 1984 (WGS84) assignment, with coincident points left undisplaced. Sixteen paired records were previously reported in Table 3 of (Liao et al. 2025); four were attributed there to (Liao et al. 2023). The present analysis uses the full-precision archive values. Records not identified in those publications retain their original archive provenance.

We summarized thermal properties by source-assigned geological era, period or subdivision, and lithology using counts, means, sample SDs, medians and ranges. The 28 Cambrian–Ordovician records labelled Mesozoic in the original era field were assigned to the Paleozoic from their recorded periods; the original entries are preserved. Qingbaikou, Nanhua, Sinian and local Neoarchean subdivisions remain source categories. Metamorphic-rock age labels do not separately identify protolith and metamorphic ages. The eight broad analogue groups aggregate finer lithological names, while Figs. 6 and 7 retain the detailed age–lithology categories. Sedimentary and metamorphic major classes follow the source hierarchy, including finer names containing granite. Grouping conventions, mapped-side comparisons and statistics are provided with the adopted-sample record (Additional file 2). These classifications can differ from the broader gneiss grouping in (Liao et al. 2025).

The original OriginPro 2025 indexed-group procedure was applied to the adopted measurements. Quartiles use the empirical distribution with averaging, and whiskers follow the 1.5 interquartile-range (IQR) rule. Arithmetic means and individual observations are displayed. Boxplot outliers remain part of the adopted dataset. The age–lithology plots contain 39 conductivity groups and 28 heat-production groups (Figs. 6 and 7); full-size layouts are provided separately (Additional file 3: Figs. S1 and S2).

Two-color patterns identify lithological categories, including the mapped general metamorphic or protolith symbols used where the library lacks a dedicated pattern. Category spacing is independent of stratigraphic thickness and geological-time duration.

Table 2. Measured thermal properties of regional rock analogue groups

Analogue group	n (k)	Mean k ± SD (W m^{-1} K^{-1})	n (A)	Mean A ± SD (μW m^{-3})
Gneiss	39	2.629 ± 0.458	21	1.644 ± 1.266
Metagranite	9	2.850 ± 0.223	5	1.326 ± 0.688
Leptynite	5	2.469 ± 0.487	5	1.172 ± 0.889
Meta-amphibolite	2	2.983 ± 0.297	1	0.122 (one value)
Granulite	1	2.631 (one value)	1	0.683 (one value)
Metagabbro	3	2.140 ± 0.361	1	0.150 (one value)
Limestone	20	2.812 ± 0.601	5	0.799 ± 0.609
Dolostone	8	3.923 ± 0.901	4	0.691 ± 0.221

Note: n, number of adopted values; SD, sample standard deviation; k, thermal conductivity; A, volumetric radiogenic heat production. Values are means ± SD; single observations are reported without SD. Sample references are listed in Additional file 1.

Table 3. Calibrated layer parameters of the lithological analogue model

Depth (km)	Lithological assignment	k_0 (W m^{-1} K^{-1})	A (μW m^{-3})
0.10–6.00	Conditional sedimentary cover	3.8000	0.7000
6.00–14.00	Gneiss analogue; effective k_0 fitted	1.9906	1.6443
14.00–22.00	Equal-volume leptynite / meta-amphibolite	2.7019	0.6471
22.00–31.06	Granulite TAN-9 analogue	2.6313	0.6831

Note: k_0, reference thermal conductivity; A, volumetric radiogenic heat production. The middle-crustal analogue contains equal volume fractions of leptynite and meta-amphibolite. L1 denotes the lithological analogue model.

3.7 Magnetic-depth constraint and conductivity calibration

We used the published Global Curie Depth Model derived from the Earth Magnetic Anomaly Grid at 2-arc-minute resolution (EMAG2) (Li et al. 2017). It averages spectral estimates from square windows with side lengths of 98.8, 195.0 and 296.4 km, advanced by 49.4, 97.5 and 98.8 km, respectively, and supplies a final 10-arcminute grid. The output spacing is a sampling interval, not independent spectral resolution. The source removed EMAG2's 4 km observation altitude to reference

depths to the geoid; we applied no second correction. Thus, a grid value provides a regional magnetic-source-bottom estimate at its stated datum, rather than a local below-ground temperature measurement.

At ZB-ZK1 (118°04′E, 36°53′N), the nearest published node gives a magnetic-source-bottom depth of 24.741037 km; Table 4 reports the borehole extractions. Both thermal models use this numerical value as the common calibration target. Bilinear interpolation gives 24.804945 km and tests grid-sampling dependence. We assigned 585°C to the selected depth following the temperature convention of the Linyi study (Liao et al. 2023). Li et al.'s approximately 550°C convention enters their thermal interpretation and heat-flow conversion, rather than the spectral depth inversion (Li et al. 2017). The 585°C linkage is therefore an explicit assumption of this study, with 550°C tested separately. The retained decimal places identify the extracted dataset value and do not express uncertainty in the magnetic bottom.

Each model is calibrated by adjusting one effective reference conductivity k_0 in the crystalline upper crust until T(24.741037 km) = 585°C. The parameter applies between the 6 km cover base and that model's upper-crustal base. Its search interval, 1.8003–3.7493 W m^{-1} K^{-1}, is the retained gneiss sample range under the laboratory-value-to-k_0 convention, not a confidence interval for the layer mean. The 100 m temperature, 64.6 mW m^{-2} upper flux, 3.8 W m^{-1} K^{-1} cover conductivity, heat-production profile, velocities, geometry, remaining conductivity parameters and assumed lithological fractions are fixed. Laboratory observations are unchanged. Baseline and calibrated values are reported together; the imposed temperature–depth match is a calibration condition and provides no independent validation.

Table 4. Magnetic depths extracted at the Zibo and Linyi reference boreholes

Site	Longitude (E)	Latitude (N)	Nearest (km)	Bilinear (km)	Role
ZB-ZK1	118°04′	36°53′	24.74	24.80	Primary Zibo calibration target
LHT-ZK1	118°24′	35°09′	27.34	27.57	Regional context; different borehole

Note: Borehole coordinates are rounded to the nearest arcminute; grid sampling uses the original coordinates. Magnetic depths are referenced to the geoid. Nearest and bilinear denote nearest-node extraction and bilinear interpolation, respectively. Magnetic grid: (Li et al. 2017); LHT-ZK1 location: (Liao et al. 2023).

4 Results

4.1 Temperature profiles and the Zibo boundary condition

The selected ZB-ZK1 profiles vary most above approximately 80–90 m (Fig. 4). Over the selected 100–200 m interval, the maximum within-depth temporal range is 0.2 °C and the median is 0.1 °C. Mean temperature increases from 15.1222 °C at 100 m to 16.7111 °C at 200 m.

Regression of the eleven mean temperatures gives G = 17.0303 °C km^{-1} and R^2 = 0.93145, reproducing the Origin fit. The intercept, 13.5323 °C, is extrapolated from the fitted interval; it is not an observed surface temperature. The conventional slope standard error is 1.5400 °C km^{-1}. With k = 3.8 W m^{-1} K^{-1}, the calculated heat flow is 64.715 mW m^{-2}, within 0.12 mW m^{-2} of the prescribed value of 64.6. A negative local gradient persists at 180–190 m despite the positive fitted gradient over the full interval.

All checked Zibo temperatures agree between Origin and the source spreadsheet. At the reported gradient of 17 °C km^{-1}, the three-sample Zibo limestone mean gives 54.00 mW m^{-2} and the two-sample Ordovician mean gives 58.37 mW m^{-2}. Using the unrounded fitted gradient gives 54.09 and 58.47 mW m^{-2}, respectively. These estimates illustrate the effect of conductivity selection. The reference model therefore retains the inventory value of 64.6, conditional on its adopted conductivity.

4.2 Regional heat flow

The 76-record compilation spans 45.2–184.3 mW m^{-2}, with an unweighted mean of 76.14, median of 71.6 and sample standard deviation of 20.84 mW m^{-2}. The adopted Zibo value exceeds 19 records, or 25% of the compilation, placing it below the median. This comparison provides no evidence for a regional high-heat-flow anomaly at the monitoring site. Mixed locations and the absence of a common measurement-quality classification prevent extrapolation to an areally uniform background.

4.3 Measured thermal-property distributions and parameter representativeness

The carbonate samples have higher mean thermal conductivity than the metamorphic samples: 3.13 ± 0.85 W m^{-1} K^{-1} (n = 28) versus 2.64 ± 0.44 (n = 59). Their mean volumetric radiogenic heat

production is lower: 0.75 ± 0.46 μW m^{-3} (n = 9) versus 1.41 ± 1.13 (n = 34; Table 5). The property distributions overlap, and the metamorphic dataset includes several felsic and mafic analogue groups (Fig. 5; Table 2).

Mean thermal conductivities of the source-assigned Neoarchean, Neoproterozoic and Paleozoic groups are 2.60, 2.82 and 3.15 W m^{-1} K^{-1}, respectively (Table 5). The medians, 2.64, 2.94 and 2.85, follow a different order. Mean heat production is 1.45, 1.33 and 0.61 μW m^{-3}; the latter two groups contain seven and eight adopted values. Figs. 6 and 7 retain the individual age–lithology categories. Of the 39 conductivity and 28 heat-production groups, 25 and 18, respectively, contain one sample; 32 conductivity groups and all heat-production groups contain fewer than five values. Under the source classification, all Paleozoic samples are sedimentary and all Neoarchean samples are metamorphic.

The conditional regional mapping places 80 samples on the Luxi side and 12 on the Jiaonan–Weihai side. Their all-rock mean thermal conductivities are similar, at 2.79 and 2.80 W m^{-1} K^{-1}. For gneiss alone, the means are 2.56 ± 0.47 (n = 28) and 2.80 ± 0.41 (n = 11), respectively. All eastern gneisses are Neoproterozoic and all Luxi gneisses are Neoarchean, so this contrast combines source age and provenance (Additional file 2).

Table 5. Thermal properties grouped by geological era and represented major rock class

Grouping	Group	n (k)	Mean k ± SD (W m^{-1} K^{-1})	n (A)	Mean A ± SD (μW m^{-3})
Era	Neoarchean	48	2.598 ± 0.442	28	1.448 ± 1.237
Era	Neoproterozoic	13	2.821 ± 0.399	7	1.327 ± 0.433
Era	Paleozoic	26	3.145 ± 0.878	8	0.611 ± 0.187
Rock class	Sedimentary	28	3.129 ± 0.852	9	0.751 ± 0.455
Rock class	Metamorphic	59	2.636 ± 0.439	34	1.411 ± 1.133

Note: n, number of adopted values; SD, sample standard deviation (n−1); k, thermal conductivity; A, volumetric radiogenic heat production. Era and major rock class summarize the same adopted samples. Group definitions are provided in Additional file 2.

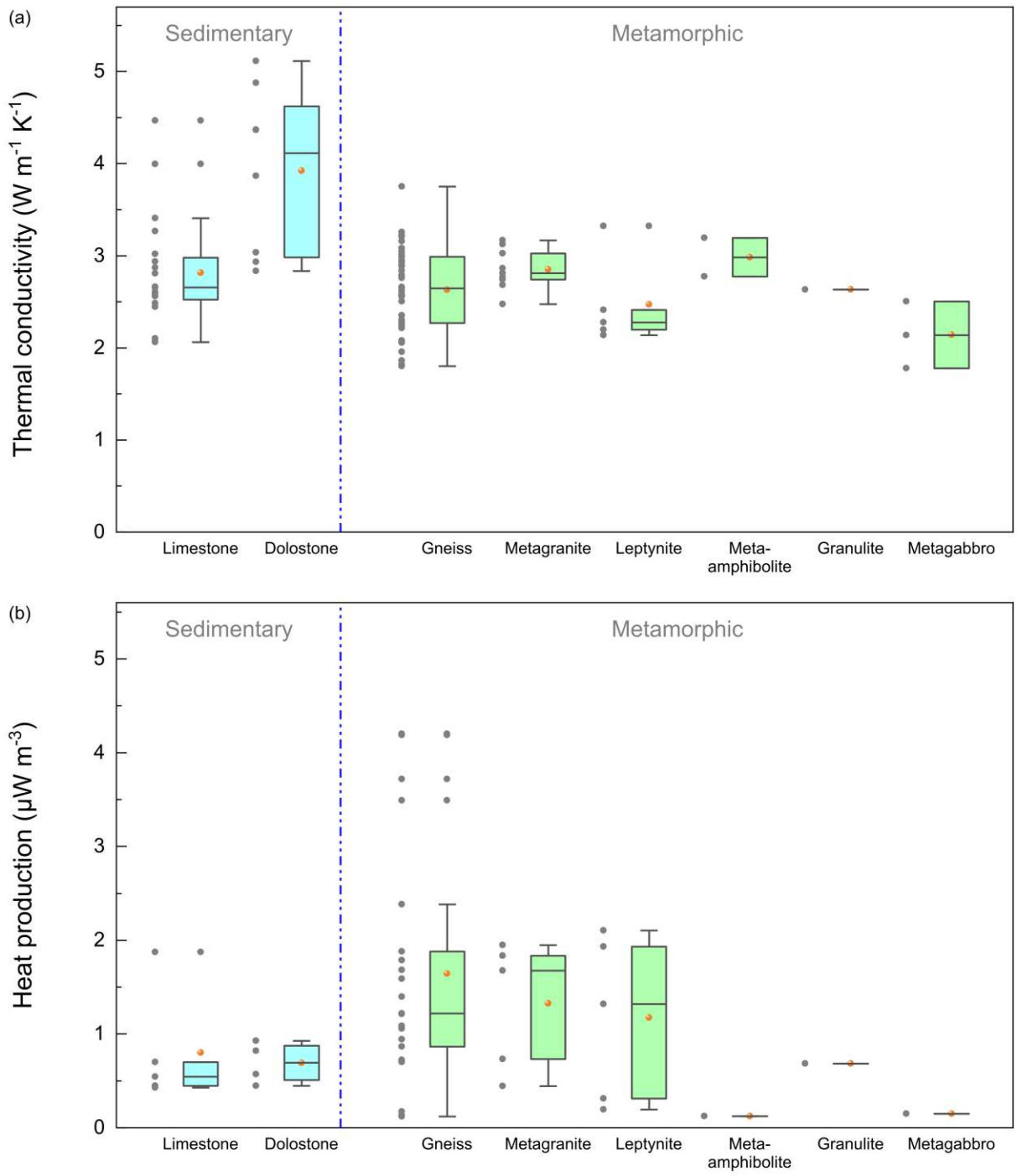


Fig. **5.** Thermal properties of the eight rock-analogue groups. a Thermal conductivity (k; n = 87). b Volumetric radiogenic heat production (A; n = 43). Boxes, interquartile range (IQR); horizontal lines, medians; whiskers, outermost observations within 1.5 IQR of the quartiles; orange marks, means; grey points, individual observations. Cyan and green denote sedimentary and metamorphic classes. Sample publication sources: (Liao et al. 2023; Liao et al. 2025).

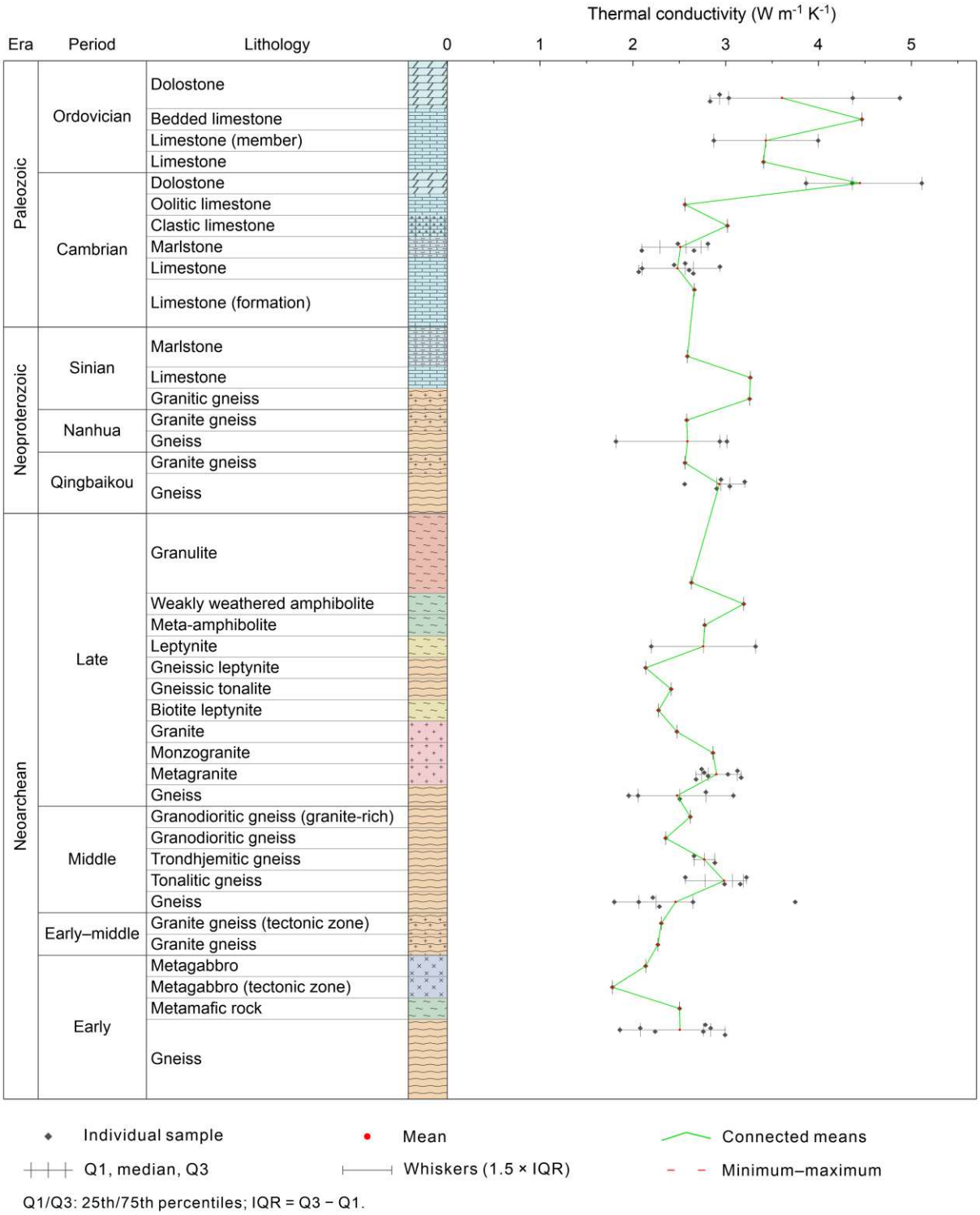


Fig. **6.** Thermal conductivity by source-assigned age and lithology. Statistical symbols are defined in the figure legend; two-color patterns identify lithological categories. Full-size layout (Additional file 3: Fig. S1).

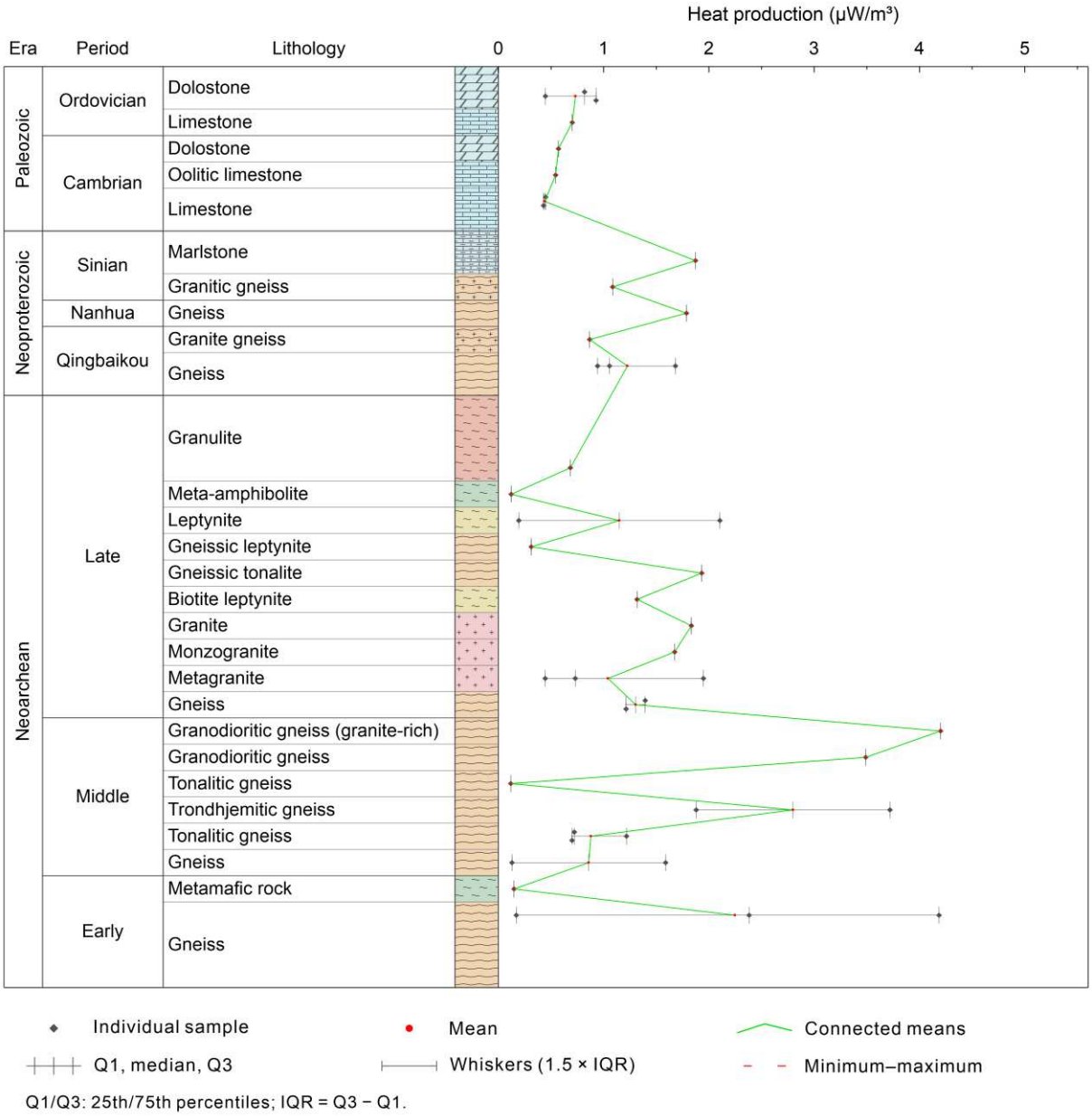


Fig. **7.** Volumetric radiogenic heat production by source-assigned age and lithology. Statistical symbols are defined in the figure legend; two-color patterns identify lithological categories. Full-size layout (Additional file 3: Fig. S2).

4.4 Conditional crustal temperatures and heat budget

The calibrated V column gives 96.2°C at 5 km, 243.3°C at 10 km, 412.0°C at 15 km and 693.7°C at the adopted 31.06 km Moho (Fig. 8; Table 6). L1 gives 678.3°C at the same model base. These deep estimates depend on the conductive model, prescribed properties and assignment of 585°C to the magnetic-depth target (Li et al. 2017); the logged temperatures constrain only the shallow interval.

Integrated radiogenic heat production over 0.1–31.06 km is 21.26 mW m^{-2} in V and 28.65 mW m^{-2} in L1. Subtracting these contributions from the prescribed upper-boundary flux of 64.6 mW m^{-2} gives

upward Moho heat fluxes of 43.34 and 35.95 mW m^{-2}, respectively, and radiogenic-to-Moho-flux ratios of 0.49 and 0.80. The budgets exclude the uppermost 100 m. Conductivity calibration leaves them unchanged because layer thicknesses and heat production are fixed.

Table 6. Temperatures in the calibrated velocity and lithological analogue models

Depth (km)	V calibrated T (°C)	L1 calibrated T (°C)
1	30.3	30.3
2	47.1	47.1
3	63.6	63.6
5	96.2	96.2
10	243.3	256.8
15	412.0	423.9
20	500.4	508.9
25	589.5	589.0
30	675.7	663.5
31.056	693.7	678.3

Note: V, velocity-based model; L1, lithological analogue model. Depths are below local ground level; the model extends from the 0.1 km anchor to the Moho.

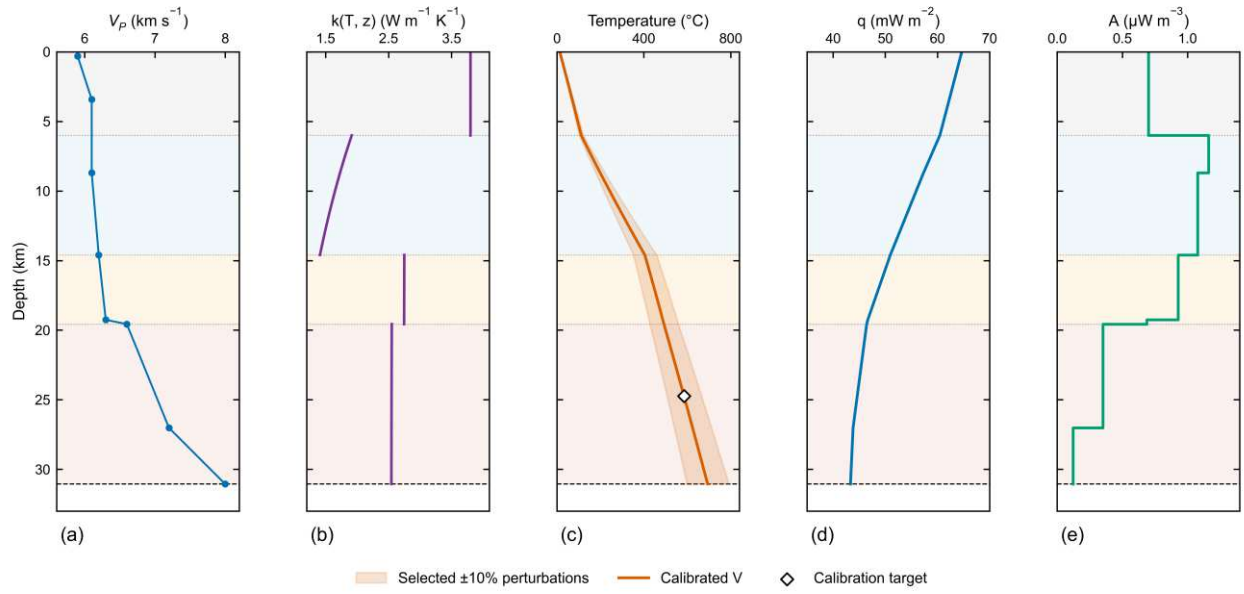


Fig. 8. Thermal structure of the calibrated velocity-based model (V). a P-wave velocity. b Thermal conductivity, k(T,z). c Temperature. d Upward conductive heat flow. e Volumetric radiogenic heat production. Background bands indicate crustal layers; dashed horizontal lines mark the 31.06 km Moho. The diamond marks the 585°C calibration target at 24.741 km. Shading shows the deterministic ±10% parameter-sensitivity envelope.

4.5 Sensitivity and numerical verification

Upper-boundary heat flow produces the largest Moho-temperature response among the separate ±10% perturbations to calibrated model V (Fig. 9). Each perturbed solution retains its changed input without refitting to the magnetic target. Independent Gauss–Legendre quadrature and ordinary differential-equation integration reproduce the primary solutions, with heat-budget residuals negligible at numerical precision. These checks verify the numerical implementation; geological uniqueness and predictive accuracy require independent evidence. The calculation stops at the selected Moho.

Nearest-node and bilinear sampling and the 550°C temperature-assignment cases yield separate parameter estimates (Table 7). Their differences describe deterministic scenario sensitivity and have no confidence-interval interpretation for magnetic depth or fitted conductivity.

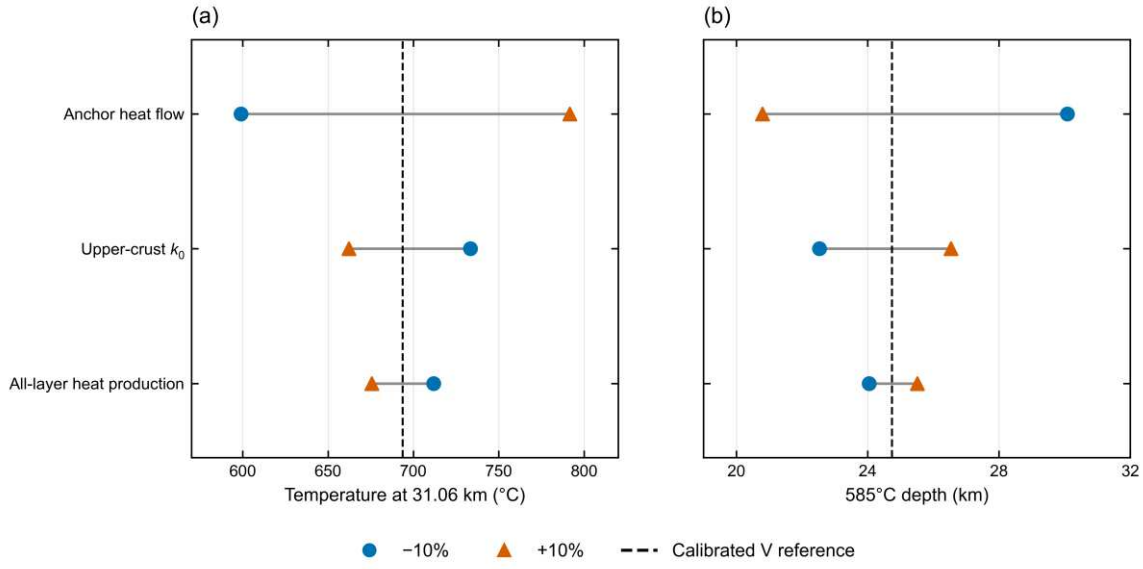


Fig. 9. Sensitivity of model V to separate ±10% input perturbations. a Moho temperature. b Depth of the 585°C isotherm. Blue circles, −10%; orange triangles, +10%. Dashed lines mark the calibrated reference (693.7°C; 24.741 km). Parameters are perturbed individually without recalibration.

4.6 Conductivity-calibrated thermal structures

Calibration lowers the effective upper-crustal thermal conductivity and raises deep temperatures in both columns (Fig. 10; Table 7). The measured sample properties remain unchanged, including the distributions in Figs. 5–7 and their full-size layouts in Additional file 3.

Matching 585°C at the common depth of 24.741 km requires upper-crustal k_0 values of 2.218 W m^{-1} K^{-1} in V and 1.991 W m^{-1} K^{-1} in L1. These are 26.1% and 24.3% below the initial values of 3.000 and 2.629 W m^{-1} K^{-1}, respectively. Both fitted values fall within the gneiss sample range used to bound the search. They describe effective layer properties within the models, while the measured sample values remain unchanged.

Calibration raises Moho temperatures from 605.9 to 693.7°C in V and from 596.0 to 678.3°C in L1. The depths of the 585°C isotherm decrease from 29.82 and 30.27 km, respectively, to the imposed 24.741 km target. Only crystalline upper-crustal k_0 is fitted, so temperature changes begin below the cover. Cover temperatures, including those at 100–200 m, remain identical before and after calibration.

Table 7. Calibration changes and magnetic sampling and temperature sensitivity

Case	UC k_0 (W m^{-1} K^{-1})	Change (%)	Moho T (°C)	Basal q (mW m^{-2})	585°C depth (km)
V Initial	3.0000	+0.0	605.9	43.34	29.82
V Primary 585°C	2.2177	-26.1	693.7	43.34	24.74
V Bilinear 585°C	2.2249	-25.8	692.6	43.34	24.80
V Nearest 550°C	2.4708	-17.6	658.3	43.34	26.76
L1 Initial	2.6289	+0.0	596.0	35.95	30.27
L1 Primary 585°C	1.9906	-24.3	678.3	35.95	24.74
L1 Bilinear 585°C	1.9963	-24.1	677.3	35.95	24.80
L1 Nearest 550°C	2.2163	-15.7	643.0	35.95	27.03

Note: UC, upper crust; k_0, reference thermal conductivity (W m^{-1} K^{-1}); T, temperature; q, upward conductive heat flux. The 550°C cases use the same 24.741037 km magnetic target. Basal heat flux remains unchanged within each model; the 100–200 m conductivity remains 3.8 W m^{-1} K^{-1}.

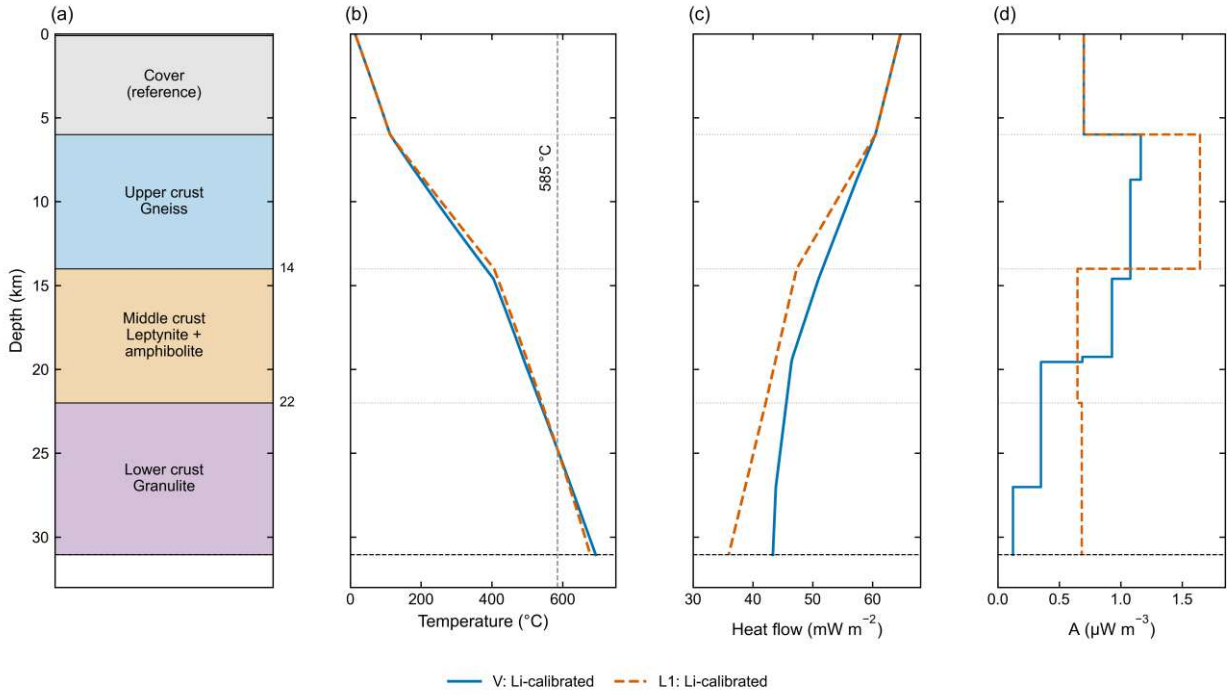


Fig. 10. Comparison of the calibrated thermal models. Blue solid lines, velocity-based model V; orange dashed lines, lithological analogue model L1. a L1 lithological analogues. b Temperature. c Upward conductive heat flow. d Volumetric radiogenic heat production. Dashed horizontal lines mark the 31.06 km Moho.

4.7 Sensitivity to magnetic-depth sampling and temperature assignment

Fig. 11 locates the monitoring well and regional transects within the magnetic-depth field; Fig. 12 compares the borehole-depth estimates. The Zibo star marks the well, and the transects provide spatial context for the published magnetic estimates.

The nearest magnetic-model node (Li et al. 2017), at 118°00′E, 36°50′N, is approximately 7.60 km from ZB-ZK1 and gives a depth of 24.741 km. Bilinear interpolation gives 24.805 km. Recalibration at the bilinear depth with the same 585°C assignment yields k_0 = 2.225 W m^{-1} K^{-1} in V and 1.996 W m^{-1} K^{-1} in L1, with Moho temperatures of 692.6 and 677.3°C, respectively. Sampling method thus has a small effect on these columns. The node–well distance describes the sampling offset; magnetic-model resolution and depth uncertainty are separate quantities.

Assigning 550°C to the same 24.741 km magnetic depth, in place of 585°C, produces a larger change. Recalibrated k_0 values are 2.471 W m^{-1} K^{-1} in V and 2.216 W m^{-1} K^{-1} in L1, with Moho temperatures of 658.3 and 643.0°C, respectively. Their 585°C isotherms lie at 26.76 and 27.03 km.

These values describe an alternative temperature-assignment scenario; they do not define confidence limits for the primary 585°C calibration.

The published LHT-ZK1 position in Linyi is 118°24′E, 35°09′N ((Liao et al. 2023); borehole inventory). The nearest-node depth from Li et al. is 27.34 km, approximately 2.16 km shallower than the thermal depth of 29.5 km reported by Liao et al. LHT-ZK1 and the present LY-ZK1 monitoring borehole are different wells. The published LHT-ZK1 coordinates have whole-arcminute precision.

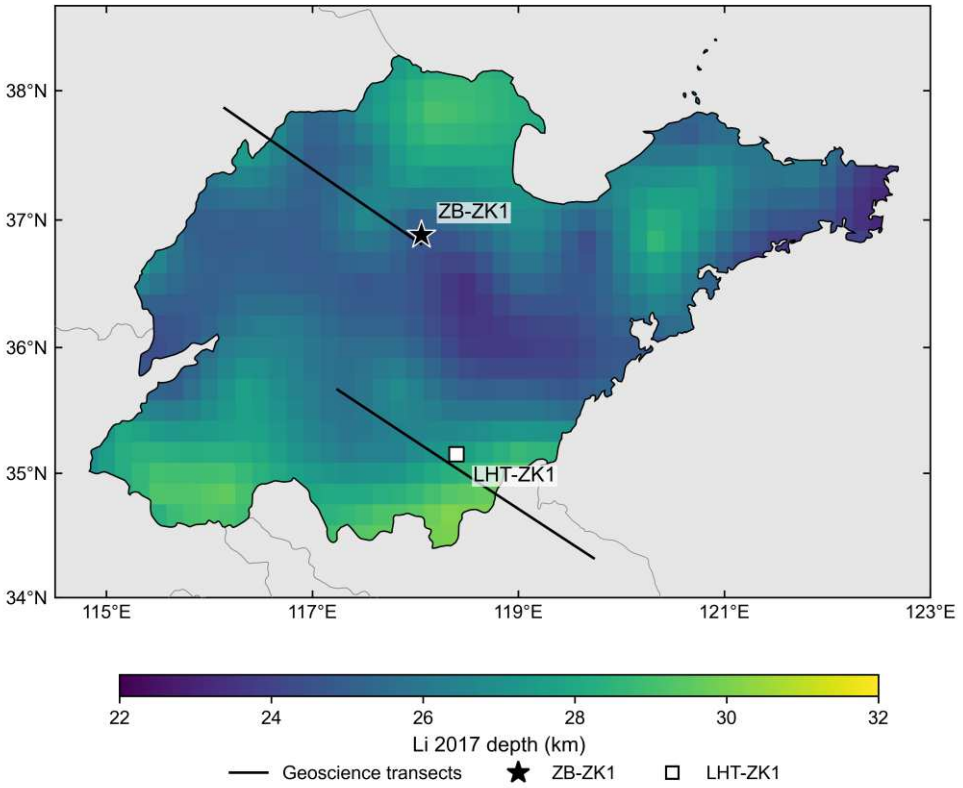


Fig. **11.** Magnetic-source bottom depths and geoscience transects across Shandong. Depths follow the 10-arcminute grid of (Li et al. 2017) and are referenced to the geoid. Star, ZB-ZK1; square, LHT-ZK1 (Liao et al. 2023); black lines, geoscience transects; grey areas, outside the Shandong boundary.

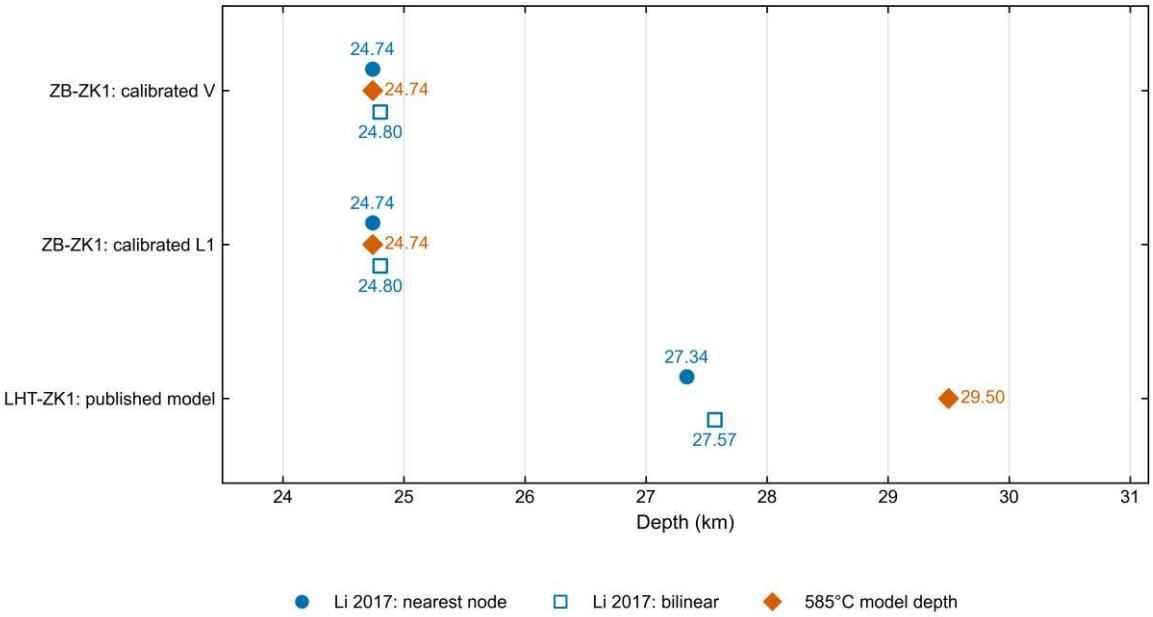


Fig. **12.** Magnetic-source and thermal-isotherm depths at the reference boreholes. V and L1 refer to Zibo; LHT-ZK1 refers to the published Linyi column (Liao et al. 2023). Magnetic depths are from (Li et al. 2017) and are geoid-referenced; thermal depths are below local ground level.

5 Discussion

5.1 Similar reported heat flow does not establish equivalent geothermal backgrounds

The Zibo observation constrains the temperature gradient over 100–200 m at ZB-ZK1. The field compilation combines 17°C km^{-1} with an adopted thermal conductivity of 3.8 W m^{-1} K^{-1} to obtain a terrestrial heat flow of 64.6 mW m^{-2}; regression of the present profiles gives 17.03°C km^{-1}. The compiled heat flow is retained as the model boundary. The repeated profiles show greater stability than the shallower interval, although residual thermal disturbances and temperatures at kilometre depths remain unconstrained. Numerical uncertainty, measurement quality and environmental disturbances require separate treatment under the International Heat Flow Commission (IHFC) heat-flow quality framework (Fuchs et al. 2023). The boundary applies to this monitoring site; its uniformity along the transect has not been established.

Linyi's reported LHT-ZK1 terrestrial heat flow of 64.9 mW m^{-2} is close to the adopted Zibo value (Liao et al. 2023). The reported gradient is higher at Linyi, 29.5°C km^{-1} compared with 17.03°C km^{-1} at Zibo, while the corresponding shallow conductivities are 2.2 and 3.8 W m^{-1} K^{-1}. The gradient and reciprocal-conductivity ratios are both approximately 1.73, as expected from Fourier's law. This

algebraic agreement depends on the reported and adopted inputs because Zibo's heat flow was calculated from conductivity and gradient. The different logging intervals, 60–1100 m at Linyi and 100–200 m at Zibo, further restrict the comparison. The similar reported fluxes therefore do not demonstrate equal true heat flow.

The adopted Zibo conductivity of 3.8 W m^{-1} K^{-1} was compared with surface-limestone samples from the regional archive. Saturation, porosity and sample condition influence the relationship between laboratory and formation-scale conductivity. Sandstone experiments document dry–saturated contrasts (Guo et al. 2017), and damaged-granite experiments show opposing effects of cracking and water saturation (Li et al. 2020). These relationships inform the interpretation of the rock analogues and the conductivity sensitivity analysis.

A representative borehole column has a different spatial scope from a geothermal-field assessment. Linyi's 64.9 mW m^{-2} is a borehole value; the published interpretation of a high geothermal background also drew on other wells, regional thermal observations and crustal–mantle structure (Liao et al. 2023). At Zibo, a value below the median of 76 regional records constrains the monitoring site alone. Terms such as high and moderate require a stated observational scale and comparison set before they can support a field-to-field contrast.

The Zibo–Linyi comparison also involves different reservoir architectures. At Zibo's northern basin–uplift transition, sedimentary-cover geometry and buried carbonate continuity affect heat storage and access (Li et al. 2013; Xiang et al. 2009). Regional studies describe sedimentary reservoirs and fault-controlled carbonate systems (Tan et al. 2019), while Zhangdian observations identify meteoric recharge and spatially variable fracture-controlled circulation (Yang et al. 2005). The Linyi succession contains carbonate and volcanic rocks, with Cretaceous andesite as a principal reservoir host, within the multibranch Yishu fault system (Liao et al. 2023). That study interprets the fault as a possible heat-transfer pathway. Assessing its relevance to Zibo requires separate tests of reservoir burial, hydraulic connectivity and advective transport alongside the conductive-background calculation. Broadly normal

heat flow in the southern Tan-Lu sector (Wang et al. 2019) provides regional context for distinguishing fault-controlled circulation from elevated heat supply; it supplies no measurements at either study well.

5.2 Thermal-property and layer choices affect the regional ranking of basal heat supply

Regional sample properties guide analogue selection, while volume-weighted deep-layer properties remain to be established. Carbonates combine relatively high thermal conductivity with lower heat production, and metamorphic groups have wider radiogenic dispersion (Figs. 5–7). For prescribed heat flow, conductivity controls thermal resistance and integrated heat production determines the residual Moho flux. Mineral composition and fabric affect conductivity (Horai 1971; Pribnow and Umsonst 1993); heterogeneity influences the relation between sample means and effective transport properties (Jorand et al. 2013). Age and lithology covary in this collection, preventing attribution of the property contrasts to age alone.

The mixing rules and depth corrections also depend on the chosen rock analogues. Sedimentary-rock tests show that predictive error varies with lithotype, pore fluid and porosity (Fuchs et al. 2013). Harmonic mixing reproduced conductivity in a tested suite of low-porosity, approximately isotropic plutonic rocks (Fuchs et al. 2018). This offers a basis for comparison with the middle-crustal mixture, whose proportions and arrangement beneath Zibo remain assumed. Conductivity decreases with temperature in several measured rock types (Miao et al. 2014; Vosteen and Schellschmidt 2003), while granite experiments document pressure effects and limits to extrapolation beyond the tested conditions (Emirov et al. 2021). These relations supply model corrections rather than in-situ property measurements. Exposed granulite-facies rocks provide lower-crustal analogues (Ray et al. 2015), with their applicability beneath Zibo dependent on the local assemblage.

The fitted k_0 values, 2.218 and 1.991 W m^{-1} K^{-1}, reconcile the assigned deep temperature with the fixed shallow boundary in V and L1. They are effective parameters of the prescribed columns; laboratory values remain unchanged. Conductivity and basement geometry can alter basin temperature without changing regional heat supply (Lemenager et al. 2018). The fitted values may therefore

638 compensate for uncertain thermal resistance within the assumed columns, precluding their
639 interpretation as uniquely recovered intrinsic upper-crustal properties.

640 Sample provenance further limits the transfer of regional properties to crustal layers. Similar all-
641 rock conductivity means on the two mapped sides conceal a gneiss contrast that also changes source
642 age, so its tectonic contribution cannot be isolated. The single heat-production values for meta-
643 amphibolite and granulite similarly provide sample analogues rather than deep-crustal population
644 distributions (Table 2). The measurements support the provenance and plausibility of the selected
645 analogues, while layer composition, volumetric proportions and in-situ properties remain conditional.
646 They cannot justify a regional-scale thermal parameter, replace calibrated effective conductivities or
647 independently validate the velocity-derived heat-production profile.

648 V and L1 use different compositional assumptions: V converts seismic structure to heat production,
649 whereas L1 assigns regional rock groups to inferred layers. Reviews show regional differences among
650 exposed granulites, xenolith suites and seismic estimates of crustal composition (Rudnick and Gao
651 2014). Joint geophysical–geochemical models propagate structural and compositional uncertainty
652 (Huang et al. 2013), and probabilistic velocity-to-lithology methods retain alternative rock types and
653 uncertainty in velocity and temperature (Takeuchi et al. 2019). V and L1 are two deterministic
654 scenarios within this broader set of possibilities; they do not sample a posterior distribution of
655 admissible crustal structures.

656 Empirical velocity relations retain compositional ambiguity. Igneous-rock compilations show
657 associations between median heat production and compositionally estimated velocity, together with
658 regional offsets, compositional exceptions and porosity and hydration effects (Hasterok and Webb
659 2017). Velocity-derived heat production is therefore a population proxy for radioelement content at
660 depth. Velocity–conductivity relations also vary with lithology, with clearer trends in porous rocks
661 than in low-porosity crystalline rocks (Mielke et al. 2017). The dispersion within granitic heat-

662 production compilations similarly prevents assignment of a universal value from a lithological name
663 alone (Artemieva et al. 2017).

664 The two property assignments reverse the inferred regional ranking of basal heat supply. At the
665 same prescribed Zibo upper flux, V and L1 yield radiogenic contributions of 21.26 and 28.65 mW m^{-2}
666 and residual Moho fluxes of 43.34 and 35.95 mW m^{-2}, respectively. Linyi's published values of 26.02
667 and 38.88 mW m^{-2} fall between them (Liao et al. 2023). Against that fixed reference, Zibo's basal flux
668 is higher under V and lower under L1. The reversal reflects combined heat-production and layer
669 assignments; these scenarios neither isolate their separate effects nor define a confidence interval.
670 Their integration intervals also differ: Zibo starts at the 100 m anchor and the published Linyi column
671 at 45 m.

672 Within each Zibo column, fixed upper flux, layer geometry and heat production determine the
673 residual Moho flux before conductivity calibration. Calibration changes the geotherm but leaves the
674 radiogenic-to-Moho-flux ratios at 0.49 and 0.80. Integrated heat production controls the residual flux,
675 and its depth distribution also affects temperature (Jaupart et al. 2016). Petrological, elevation and
676 xenolith-thermobarometric constraints can provide independent tests of the partition (Hasterok and
677 Chapman 2011). Reduced heat flow, Moho heat flux and heat supply at the lithosphere base have
678 different definitions (Furlong and Chapman 2013; Jaupart and Mareschal 2007). The calculated Moho
679 residual alone cannot locate the lithosphere–asthenosphere boundary or diagnose current magmatism
680 or mantle upwelling.

681 Earlier North China modelling showed that applying one regional heat-production structure
682 everywhere could produce unreasonable thermal results (Zang et al. 2002). Its Moho-temperature
683 range of approximately 450–750°C gives regional context rather than an independent measurement
684 beneath Zibo. The present calculation quantifies the structural and property dependence of the Zibo
685 column and its comparison with Linyi.

5.3 Magnetic calibration and the limits of cross-field temperature comparison

Using the magnetic bottom to constrain a geotherm requires a thermal interpretation of magnetization loss. The EMAG2-derived product estimates the basal limit of effective magnetization under assumptions about source geometry and spatial statistics (Li et al. 2017). Composition can also define that limit (Mayhew 1985; Ross et al. 2006), and spectral fitting and source-statistical choices affect the estimated depth (Ravat et al. 2007; Bouligand et al. 2009). The regional magnetic depth is therefore assigned a temperature explicitly for calibration. The assigned temperature provides an external condition for calibrating the conductive models.

The primary target uses the nearest-node depth of 24.741 km; bilinear sampling gives 24.805 km. Their difference measures extraction sensitivity, while inversion uncertainty requires separate assessment. The 10-arcminute grid samples estimates derived from approximately 99–296 km windows (Li et al. 2017), giving adjacent cells overlapping regional support rather than independent borehole-scale information. Grid sampling and the assignments of 585°C and 550°C test different assumptions and are reported separately. Magnetic depths are geoid-referenced and thermal depths are below local ground level. The selected depth is used as the nominal calibration target.

Both Zibo columns satisfy T = 585°C at 24.741 km and give Moho temperatures of 693.7°C in V and 678.3°C in L1. The shared target fits one effective conductivity in each assumed structure, leaving the structure and source budget unresolved. Temperature–depth-constrained conductive solutions depend on their admissible properties and boundary conditions (Ravat et al. 2016). Other conductivity distributions, heat-production assignments and non-conductive processes remain possible after this single-parameter fit. Independent temperatures are therefore needed to test the predictive accuracy of these internally consistent calibrations.

At the nominal LHT-ZK1 location, the magnetic product gives 27.337 km by nearest-node extraction and 27.568 km by bilinear interpolation. The nearest-node difference from Zibo is approximately 2.60 km. Both estimates belong to one regional product with overlapping spectral

support, so they do not independently resolve a local depth contrast. A separate difference of approximately 4.76 km compares Linyi's published thermal 585°C depth of 29.5 km with Zibo's imposed 24.741 km target, using different modelling procedures (Liao et al. 2023). V and L1 share the same Zibo extraction and therefore one spatial sample. LHT-ZK1 is distinct from the shallow LY monitoring well.

The calibrated Zibo Moho temperatures exceed Linyi's published 614.8°C (Liao et al. 2023). The columns differ in shallow observations, layering, conductivity treatment and magnetic calibration, and Linyi has not been recalculated with the present solver. A controlled comparison would harmonize property definitions, integration, vertical references and magnetic-temperature assignments while retaining each site's independently defined shallow boundary. Linyi is consequently a published regional reference for this analysis. The conditional temperature and magnetic-depth differences cannot establish a measured tectonic contrast, mantle upwelling or different fault-mediated heat transfer.

5.4 Implications for geothermal assessment and independent tests

At Zibo's northern basin–uplift transition, a common shallow heat-flow boundary and deep calibration target permit different basal heat contributions. This restricts direct transfer of the Linyi column and identifies the formation properties and deeper temperatures needed to distinguish the alternatives. Thermal resistance controls the gradient–flux relation; heat-production and layer assignments control the residual Moho flux. Burial, cover properties and groundwater circulation must also be assessed when relating the adopted moderate conductive flux to local geothermal occurrences. The present column leaves reservoir-scale advective transport unquantified.

Conductivity calibration retains uncertainty in the inherited structure. The geophysical and lithological interpretations place the local Moho at different depths, and the supplied velocity nodes allow more than one thermal-layer assignment. The adopted 31.06 km column is one reference realization (Ma et al. 1991a). A single limestone conductivity represents the heterogeneous succession

736 above 6 km, simplifying its thermal resistance. This kilometre-scale package is distinct from the
737 inferred shallow Quaternary cover. Both representative wells obtain deep information from nearby
738 regional transects, whose crossings of structural divisions do not change the wells' positions. The
739 transferred sections provide inherited structural context without resolving a two-dimensional thermal
740 field.

741 The separate ±10% perturbations quantify local sensitivity around one calibrated conductive
742 structure, with no refitting; they do not sample the full distribution of admissible columns (Chapman
743 1986). The common predictions of approximately 47°C at 2 km and 96°C at 5 km follow from the
744 shared boundary and cover properties. Their agreement is an expected consequence of that
745 representation, while independent temperatures at these depths remain unavailable. The conductive
746 estimates leave flowing-water temperature, transmissivity and sustainable yield unresolved.

747 The sample distribution points to specific additions: paired thermal-conductivity and radioelement
748 measurements from documented formations, larger mafic and granulite suites, and gneiss comparisons
749 matched for source age and lithology across structural settings. Collection mode, petrographic
750 classification and the basis of age assignments should accompany those measurements. Such sampling
751 would directly address the present provenance and property ambiguities and clarify the transfer from
752 regional samples to deep layers.

753 Formation-specific saturated thermal conductivity, radioelement measurements tied to borehole
754 stratigraphy and deeper equilibrium temperature logs would provide the strongest tests of the
755 alternatives. Joint temperature, conductivity and heat-production measurements in a deep scientific
756 borehole illustrate how a vertical source budget can be tested (Wang et al. 2023); its high-radioactivity
757 lithologies cannot be inferred beneath Zibo from that example. Hydraulic and geochemical
758 measurements should examine carbonate–fault connectivity and lateral heat redistribution separately.
759 A matched Zibo–Linyi analysis could then distinguish geometric from material-property effects before

applying a common magnetic-temperature calibration. Together, these observations would test regional heat availability and the pathways supplying accessible geothermal heat.

6 Conclusions

The selected ZB-ZK1 interval gives a geothermal gradient of 17.03°C km^{-1}. With the adopted conductivity, the prescribed terrestrial heat flow is 64.6 mW m^{-2}, below the median of the regional compilation. This conditional site estimate provides no evidence for a regional high-heat-flow anomaly. Carbonate burial and fault-controlled groundwater circulation require separate assessment to explain the reported warm-water occurrences.

The calibrated V and L1 columns yield effective upper-crustal reference conductivities of 2.2177 and 1.9906 W m^{-1} K^{-1} and Moho temperatures of 693.7 and 678.3°C, respectively. These thermal structures depend on the adopted composition and layering. Regional samples support the analogue choices, while covarying age, lithology and provenance and sparse mafic sampling restrict their transfer to deep-layer properties.

The prescribed deep properties and layers reverse the inferred Zibo–Linyi basal-flux ranking. With a common imposed 585°C depth of 24.74 km, V and L1 retain radiogenic contributions of 21.26 and 28.65 mW m^{-2} and residual Moho fluxes of 43.34 and 35.95 mW m^{-2}, respectively. Linyi's published 38.88 mW m^{-2} lies between them. Conductivity calibration narrows the geotherms while fixed heat production leaves source partitioning unresolved. This ranking compares alternative Zibo scenarios against the published Linyi column; the two fields have not undergone a matched recalculation.

Upper-boundary heat flow produces the largest Moho-temperature response among the ±10% perturbations. Replacing the 585°C assignment with 550°C at the same magnetic depth gives recalibrated Moho temperatures of 658.3 and 643.0°C. Magnetic-temperature correspondence has a substantial effect on the inferred thermal background, while nearest-node versus bilinear sampling has a smaller effect in these scenarios.

Under the adopted conductivity, the shared cover gives conductive temperatures of approximately 47°C at 2 km and 96°C at 5 km. Assessing recoverable heat, flowing-water temperature and sustainable yield requires formation-specific thermal measurements, deeper equilibrium logs and fault–reservoir characterization. These independent observations would distinguish regional heat supply from local redistribution and test transfer between the fields beyond their shared magnetic calibration.

Declarations

Availability of data and materials

The adopted sample register and rock-property statistics are provided without sample coordinates (Additional files 1 and 2). Full-size age–lithology plots are provided in Additional file 3 (Figs. S1 and S2). The magnetic-depth dataset is available with its source article (Li et al. 2017). Supporting borehole records, velocity nodes, model parameters, calibration and sensitivity inputs and outputs, analysis scripts and the coordinate-bearing sample register are available from the corresponding author on reasonable request.

Competing interests

The authors declare that they have no competing interests.

Funding

This work was supported by the Deep Earth Probe and Mineral Resources Exploration–National Science and Technology Major Project (grant no. 2024ZD1004008) and the China Geological Survey, Ministry of Natural Resources (grant no. DD20221676).

Reference

Artemieva IM, Thybo H, Jakobsen K, Sørensen NK, Nielsen LSK (2017) Heat production in granitic rocks: Global analysis based on a new data compilation GRANITE2017. Earth-Science Reviews 172:1-26. doi:10.1016/j.earscirev.2017.07.003

Bouligand C, Glen JMG, Blakely RJ (2009) Mapping Curie temperature depth in the western United States with a fractal model for crustal magnetization. Journal of Geophysical Research: Solid Earth 114 (B11):B11104. doi:10.1029/2009JB006494

812 Čermák V, Bodri L, Rybach L, Buntebarth G (1990) Relationship between seismic velocity and heat
813 production: comparison of two sets of data and test of validity. Earth and Planetary Science
814 Letters 99 (1–2):48-57. doi:10.1016/0012-821X(90)90069-A
815 Chapman DS (1986) Thermal gradients in the continental crust. In: Dawson JB, Carswell DA, Hall J,
816 Wedepohl KH (eds) The Nature of the Lower Continental Crust, vol 24. Geological Society,
817 London, Special Publications. Geological Society, London, pp 63-70.
818 doi:10.1144/gsl.sp.1986.024.01.07
819 Christensen NI, Mooney WD (1995) Seismic velocity structure and composition of the continental
820 crust: A global view. Journal of Geophysical Research: Solid Earth 100 (B6):9761-9788.
821 doi:10.1029/95JB00259
822 Emirov SN, Aliverdiev AA, Beybalaev VD, Amirova AA (2021) On the temperature and pressure
823 dependences of the effective thermal conductivity of granites. Thermal Science 25 (4):2493-
824 2501. doi:10.2298/TSCI200408176E
825 Fang B (2006) Perspective Prognosis on Geothermal Resource in Synthetic Information in Shandong
826 Province. PhD thesis, Jilin University, Changchun
827 Fuchs S, Förster H-J, Braune K, Förster A (2018) Calculation of Thermal Conductivity of Low-Porous,
828 Isotropic Plutonic Rocks of the Crust at Ambient Conditions From Modal Mineralogy and
829 Porosity: A Viable Alternative for Direct Measurement? Journal of Geophysical Research:
830 Solid Earth 123 (10):8602-8614. doi:10.1029/2018jb016287
831 Fuchs S, Norden B, Neumann F, Kaul N, Tanaka A, Kukkonen IT, Pascal C, Christiansen R, Gola G,
832 Šafanda J, Espinoza-Ojeda OM, Marzan I, Rybach L, Balkan-Pazvantoğlu E, Ramalho EC,
833 Dědeček P, Negrete-Aranda R, Balling N, Poort J, Wang Y, Jõeleht A, Rajver D, Gao X, Liu S,
834 Harris R, Richards M, McLaren S, Chiozzi P, Nunn J, Madon M, Beardsmore G, Funnell R,
835 Duerrast H, Jennings S, Elger K, Pauselli C, Verdoya M (2023) Quality-assurance of heat-flow
836 data: The new structure and evaluation scheme of the IHFC Global Heat Flow Database.
837 Tectonophysics 863:229976. doi:10.1016/j.tecto.2023.229976
838 Fuchs S, Schütz F, Förster H-J, Förster A (2013) Evaluation of common mixing models for calculating
839 bulk thermal conductivity of sedimentary rocks: Correction charts and new conversion
840 equations. Geothermics 47:40-52. doi:10.1016/j.geothermics.2013.02.002
841 Furlong KP, Chapman DS (2013) Heat Flow, Heat Generation, and the Thermal State of the
842 Lithosphere. Annual Review of Earth and Planetary Sciences 41 (1):385-410.
843 doi:10.1146/annurev.earth.031208.100051
844 Gao Z, Hao M, Liu J, Li Q, Tan M, Niu Y (2023) A Comprehensive Study on the Hydrogeochemical
845 and Isotope Characteristics and Genetic Mechanism of Geothermal Water in the Northern Jinan
846 Region. Energies 16 (22):7658. doi:10.3390/en16227658
847 Guo PY, Zhang N, He MC, Bai BH (2017) Effect of water saturation and temperature in the range of
848 193 to 373K on the thermal conductivity of sandstone. Tectonophysics 699:121-128.
849 doi:10.1016/j.tecto.2017.01.024
850 Hasterok D, Chapman DS (2011) Heat production and geotherms for the continental lithosphere. Earth
851 and Planetary Science Letters 307 (1-2):59-70. doi:10.1016/j.epsl.2011.04.034
852 Hasterok D, Webb J (2017) On the radiogenic heat production of igneous rocks. Geoscience Frontiers
853 8 (5):919-940. doi:10.1016/j.gsf.2017.03.006
854 He Z, Feng J, Luo J, Zeng Y (2023) Distribution, exploitation, and utilization of intermediate-to-deep
855 geothermal resources in eastern China. Energy Geoscience 4 (4):100187.
856 doi:10.1016/j.engeos.2023.100187
857 Horai K-i (1971) Thermal conductivity of rock-forming minerals. Journal of Geophysical Research 76
858 (5):1278-1308. doi:10.1029/JB076i005p01278

Huang Y, Chubakov V, Mantovani F, Rudnick RL, McDonough WF (2013) A reference Earth model for the heat-producing elements and associated geoneutrino flux. Geochemistry, Geophysics, Geosystems 14 (6):2003-2029. doi:10.1002/ggge.20129
Jaupart C, Mareschal J-C (2007) 6.05 - Heat Flow and Thermal Structure of the Lithosphere. In: Schubert G (ed) Treatise on Geophysics, vol 6. Elsevier, pp 217-251. doi:10.1016/B978-044452748-6.00104-8
Jaupart C, Mareschal J-C, Iarotsky L (2016) Radiogenic heat production in the continental crust. Lithos 262:398-427. doi:10.1016/j.lithos.2016.07.017
Jiang G, Hu S, Shi Y, Zhang C, Wang Z, Hu D (2019) Terrestrial heat flow of continental China: Updated dataset and tectonic implications. Tectonophysics 753:36–48. doi:10.1016/j.tecto.2019.01.006
Jiang G, Tang X, Rao S, Gao P, Zhang L, Zhao P, Hu S (2016) High-quality heat flow determination from the crystalline basement of the south-east margin of North China Craton. Journal of Asian Earth Sciences 118:1-10. doi:10.1016/j.jseaes.2016.01.009
Jorand R, Vogt C, Marquart G, Clauser C (2013) Effective thermal conductivity of heterogeneous rocks from laboratory experiments and numerical modeling. Journal of Geophysical Research: Solid Earth 118 (10):5225-5235. doi:10.1002/jgrb.50373
Lachenbruch AH (1970) Crustal temperature and heat production: Implications of the linear heat-flow relation. Journal of Geophysical Research 75 (17):3291-3300. doi:10.1029/JB075i017p03291
Lemenager A, O'Neill C, Zhang S, Evans M (2018) The effect of temperature-dependent thermal conductivity on the geothermal structure of the Sydney basin. Geothermal Energy 6:6. doi:10.1186/s40517-018-0092-5
Li C-F, Lu Y, Wang J (2017) A global reference model of Curie-point depths based on EMAG2. Scientific Reports 7:45129. doi:10.1038/srep45129
Li L, Zhong D, Shi X, Tang Z, Hu Q, Xu Y, Li Z (2009) Late Mesozoic–Cenozoic décollement structure and its deep geological background in western Shandong, China. Progress in Natural Science 19 (5):603-613. doi:10.1016/j.pnsc.2008.08.006
Li L, Zhong D, Yang C, Shi X, Zhao L, Dong D (2013) The coupling relationship between the west Shandong rise and the Jiyang depression, China. Journal of Earth Science 24 (4):626-644. doi:10.1007/s12583-013-0352-z
Li P, He Z, Hu Z, Zhang Y, Feng J (2024) Conditions for the enrichment of karst hydrothermal resources in Bohai Bay Basin. Energy Geoscience 5 (1):100234. doi:10.1016/j.engeos.2023.100234
Li Z-W, Zhang Y-J, Gong Y-H, Zhu G-Q (2020) Influences of mechanical damage and water saturation on the distributed thermal conductivity of granite. Geothermics 83:101736. doi:10.1016/j.geothermics.2019.101736
Liao Y, Liu Y, Liu F, Wei S, Duan H (2022) Lithospheric Thermal Structure in Jinggangshan City: Implications for High Geothermal Background. Frontiers in Earth Science 10:854232. doi:10.3389/feart.2022.854232
Liao Y, Zhang W, Rong Y, Li L, Hu G (2025) Geothermal distribution and evolution of fault-controlled Linyi geothermal system: Constrained from hydrogeochemical composition and numerical simulation. Geothermics 125:103155. doi:10.1016/j.geothermics.2024.103155
Liao Y, Zhang W, Rong Y, Liu F, Wei S, Li L, Zhao Z, Li M (2023) A high geothermal setting in the Linyi geothermal field: Evidence from the lithospheric thermal structure. Energy Exploration & Exploitation 41 (6):1899–1918. doi:10.1177/01445987231185850
Liu Y, Zhang T, Zhang H, Jin X, Ji X, Li X, Meng M, Li Z, Liu J, Li X (2023) Characteristics of the stratigraphic reservoirs and caprocks of the geothermal resources in the Northwestern Shandong region. Energy Exploration & Exploitation 41 (5):1519-1538. doi:10.1177/01445987231183181

908 Lund JW, Huttrer GW, Toth AN (2022) Characteristics and trends in geothermal development and use,
909 1995 to 2020. Geothermics 105:102522. doi:10.1016/j.geothermics.2022.102522
910 Lund JW, Toth AN (2021) Direct utilization of geothermal energy 2020 worldwide review.
911 Geothermics 90:101915. doi:10.1016/j.geothermics.2020.101915
912 Ma X, Liu C, Liu G (1991a) Geoscience transect from Xiangshui, Jiangsu, to Mandula, Inner
913 Mongolia: Map and explanatory notes, scale 1:1,000,000. Geological Publishing House,
914 Beijing
915 Ma X, Liu C, Liu G (1991b) Xiangshui (Jiangsu province) to Mandal (Nei Monggol) geoscience
916 transect. Acta Geologica Sinica 65 (3):199–215
917 Ma Y (2023) Deep geothermal resources in China: Potential, distribution, exploitation, and utilization.
918 Energy Geoscience 4 (4):100209. doi:10.1016/j.engeos.2023.100209
919 Mayhew M (1985) Curie isotherm surfaces inferred from high-altitude magnetic anomaly data. Journal
920 of Geophysical Research: Solid Earth 90 (B3):2647-2654. doi:10.1029/JB090iB03p02647
921 Miao SQ, Li HP, Chen G (2014) Temperature dependence of thermal diffusivity, specific heat
922 capacity, and thermal conductivity for several types of rocks. Journal of Thermal Analysis and
923 Calorimetry 115 (2):1057-1063. doi:10.1007/s10973-013-3427-2
924 Mielke P, Bär K, Sass I (2017) Determining the relationship of thermal conductivity and
925 compressional wave velocity of common rock types as a basis for reservoir characterization.
926 Journal of Applied Geophysics 140:135-144. doi:10.1016/j.jappgeo.2017.04.002
927 Moeck IS (2014) Catalog of geothermal play types based on geologic controls. Renewable and
928 Sustainable Energy Reviews 37:867–882. doi:10.1016/j.rser.2014.05.032
929 Pribnow D, Umsonst T (1993) Estimation of thermal conductivity from the mineral composition:
930 Influence of fabric and anisotropy. Geophysical Research Letters 20 (20):2199-2202.
931 doi:10.1029/93GL02135
932 Qi J, Yang Q (2010) Cenozoic structural deformation and dynamic processes of the Bohai Bay basin
933 province, China. Marine and Petroleum Geology 27 (4):757-771.
934 doi:10.1016/j.marpetgeo.2009.08.012
935 Ravat D, Morgan P, Lowry AR (2016) Geotherms from the temperature-depth–constrained solutions
936 of 1-D steady-state heat-flow equation. Geosphere 12 (4):1187-1197. doi:10.1130/GES01235.1
937 Ravat D, Pignatelli A, Nicolosi I, Chiappini M (2007) A study of spectral methods of estimating the
938 depth to the bottom of magnetic sources from near-surface magnetic anomaly data.
939 Geophysical Journal International 169 (2):421-434. doi:10.1111/j.1365-246X.2007.03305.x
940 Ray L, Förster H-J, Förster A, Fuchs S, Naumann R, Appelt O (2015) Tracking the thermal properties
941 of the lower continental crust: Measured versus calculated thermal conductivity of high-grade
942 metamorphic rocks (Southern Granulite Province, India). Geothermics 55:138-149.
943 doi:10.1016/j.geothermics.2015.01.007
944 Ross HE, Blakely RJ, Zoback MD (2006) Testing the use of aeromagnetic data for the determination
945 of Curie depth in California. Geophysics 71 (5):L51-L59. doi:10.1190/1.2335572
946 Rudnick RL, Gao S (2014) Composition of the Continental Crust. In: Holland HD, Turekian KK (eds)
947 Treatise on Geochemistry, vol 4. 2 edn. Elsevier, pp 1-51. doi:10.1016/b978-0-08-095975-
948 7.00301-6
949 Shi M, Kang F, Yin T, Gao S, Sui H, Guo X, Yu X (2022) Occurrence Mechanism of Convective
950 Geothermal Systems in Jiaodong Peninsula, China. Frontiers in Earth Science 10:898414.
951 doi:10.3389/feart.2022.898414
952 Takeuchi N, Ueki K, Iizuka T, Nagao J, Tanaka A, Enomoto S, Shirahata Y, Watanabe H, Yamano M,
953 Tanaka HKM (2019) Stochastic modeling of 3-D compositional distribution in the crust with
954 Bayesian inference and application to geoneutrino observation in Japan. Physics of the Earth
955 and Planetary Interiors 288:37-57. doi:10.1016/j.pepi.2019.01.002

Tan X-b, Wei S-m, Bo B-y, Jiang D-q (2019) Analysis of occurrence characteristics of geothermal resources and its relation to control structures in Zibo City, China. Journal of Groundwater Science and Engineering 7 (1):70–76. doi:10.19637/j.cnki.2305-7068.2019.01.007

Vosteen H-D, Schellschmidt R (2003) Influence of temperature on thermal conductivity, thermal capacity and thermal diffusivity for different types of rock. Physics and Chemistry of the Earth, Parts A/B/C 28 (9–11):499-509. doi:10.1016/S1474-7065(03)00069-X

Wang G, Zhang W, Liang J, Lin W, Liu Z, Wang W (2017) Evaluation of Geothermal Resources Potential in China. Acta Geoscientica Sinica 38 (4):449-459. doi:10.3975/cagsb.2017.04.02

Wang J, Jin M, Jia B, Kang F (2015) Hydrochemical characteristics and geothermometry applications of thermal groundwater in northern Jinan, Shandong, China. Geothermics 57:185-195. doi:10.1016/j.geothermics.2015.07.002

Wang Y, Furlong K, Fuchs S, He L, Hu S (2023) Terrestrial Heat Flow Variation With Depth Caused by Anomalously High Radiogenic Heat Production. Geophysical Research Letters 50 (8):e2022GL102312. doi:10.1029/2022GL102312

Wang Y, Hu S, Nie D, Zhang K, Jiang G, Wang Z (2019) Is the Tan-Lu fault zone a thermal anomaly belt: Constraints from heat flow in its southern section. Chinese Journal of Geophysics 62 (8):3078-3094. doi:10.6038/cjg2019N0003

Wang Y, Liu S, Chen C, Jiang G, Wu J, Guo L, Wang Y, Zhang H, Wang Z, Jiang X, Zhu C, Zuo Y, Hu J, Zhang C, He L, Hu S, Pang Z, Wang J (2024) Compilation of terrestrial heat flow data in continental China (5th edition). Chinese Journal of Geophysics 67 (11):4233-4265. doi:10.6038/cjg2024S0284

Xiang Q-k, Han J-j, Li C-l, Zhang L-x (2009) Reseach on Forming Condition of Geothermal Resource in Zhangdian Region of Zibo City. Shandong Land and Resources 25 (9):33–36

Xu S, Ren X (2016) Geothermal reservoir characteristics of the Zhangdian geothermal field and their relationship with controlling structures. Diqiu (10):91

Yang F, Santosh M, Glorie S, Jepson G, Xue F, Kim SW (2020) Meso-Cenozoic multiple exhumation in the Shandong Peninsula, eastern North China Craton: Implications for lithospheric destruction. Lithos 370-371:105597. doi:10.1016/j.lithos.2020.105597

Yang P (2020) Research on Geophysical interpretation of Sedimentary Geothermal Resources in Syncline Basin. MSc thesis, Jilin University, Changchun

Yang S, Zhang H-d, Li W-z, Wu L (2005) Genesis of geothermal anomaly in Southern Zhangdian District of Zibo City. Hydrogeology & Engineering Geology 32 (3):59–62

Zang S-X, Liu Y-G, Ning J-Y (2002) Thermal Structure of the Lithosphere in North China. Chinese Journal of Geophysics 45 (1):56–66

Zhang Y, Dong S, Shi W (2003) Cretaceous deformation history of the middle Tan-Lu fault zone in Shandong Province, eastern China. Tectonophysics 363 (3-4):243-258. doi:10.1016/s0040-1951(03)00039-8

Zhu J, Hu K, Lu X, Huang X, Liu K, Wu X (2015) A review of geothermal energy resources, development, and applications in China: Current status and prospects. Energy 93:466-483. doi:10.1016/j.energy.2015.08.098

Zuo Q, Ye T, Feng Y, Ge Z, Wang Y (2018) Spatial Database of Serial Suite-Tectonic Map-sheets of Mainland China (1:250,000). Geology in China 45 (S1):1–26. doi:10.12029/gc2018Z101

Supplementary Files

This is a list of supplementary files associated with this preprint. Click to download.

- Additionalfile1.xlsx
- Additionalfile2.xlsx